

AFRL-ML-WP-TR-2004-4232

**MICROSTRUCTURAL FAILURE
PHYSICS FOR STRUCTURAL
FAILURE PROGNOSIS AND
DIAGNOSIS**



**Donald A. Shockey
Jeffrey W. Simons
Takao Kobayashi
Dennis Grishin**

**SRI International
333 Ravenswood Avenue
Menlo Park, CA 94025**

DECEMBER 2003

Final Report for 18 April 2002 – 31 December 2003

Approved for public release; distribution is unlimited.

STINFO FINAL REPORT

**MATERIALS AND MANUFACTURING DIRECTORATE
AIR FORCE RESEARCH LABORATORY
AIR FORCE MATERIEL COMMAND
WRIGHT-PATTERSON AIR FORCE BASE, OH 45433-7750**

NOTICE

USING GOVERNMENT DRAWINGS, SPECIFICATIONS, OR OTHER DATA INCLUDED IN THIS DOCUMENT FOR ANY PURPOSE OTHER THAN GOVERNMENT PROCUREMENT DOES NOT IN ANY WAY OBLIGATE THE U.S. GOVERNMENT. THE FACT THAT THE GOVERNMENT FORMULATED OR SUPPLIED THE DRAWINGS, SPECIFICATIONS, OR OTHER DATA DOES NOT LICENSE THE HOLDER OR ANY OTHER PERSON OR CORPORATION; OR CONVEY ANY RIGHTS OR PERMISSION TO MANUFACTURE, USE, OR SELL ANY PATENTED INVENTION THAT MAY RELATE TO THEM.

THIS REPORT IS RELEASABLE TO THE NATIONAL TECHNICAL INFORMATION SERVICE (NTIS). AT NTIS, IT WILL BE AVAILABLE TO THE GENERAL PUBLIC, INCLUDING FOREIGN NATIONALS.

THIS TECHNICAL REPORT HAS BEEN REVIEWED AND IS APPROVED FOR PUBLICATION.

/s/

JAY R. JIRA, Project Engineer
Behavior/Life Prediction Section
Metals, Ceramics & NDE Division

/s/

ROLLIE E. DUTTON, Chief
Metals Branch
Metals, Ceramics & NDE Division

/s/

GERALD J. PETRAK, Assistant Chief
Metals, Ceramics & NDE Division
Materials & Manufacturing Directorate

DO NOT RETURN COPIES OF THIS REPORT UNLESS CONTRACTUAL OBLIGATIONS OR NOTICE ON A SPECIFIC DOCUMENT REQUIRES ITS RETURN.

REPORT DOCUMENTATION PAGE				Form Approved OMB No. 0704-0188	
<p>The public reporting burden for this collection of information is estimated to average 1 hour per response, including the time for reviewing instructions, searching existing data sources, gathering and maintaining the data needed, and completing and reviewing the collection of information. Send comments regarding this burden estimate or any other aspect of this collection of information, including suggestions for reducing this burden, to Department of Defense, Washington Headquarters Services, Directorate for Information Operations and Reports (0704-0188), 1215 Jefferson Davis Highway, Suite 1204, Arlington, VA 22202-4302. Respondents should be aware that notwithstanding any other provision of law, no person shall be subject to any penalty for failing to comply with a collection of information if it does not display a currently valid OMB control number. PLEASE DO NOT RETURN YOUR FORM TO THE ABOVE ADDRESS.</p>					
1. REPORT DATE (DD-MM-YY) December 2003		2. REPORT TYPE Final		3. DATES COVERED (From - To) 04/18/2002 – 12/31/2003	
4. TITLE AND SUBTITLE MICROSTRUCTURAL FAILURE PHYSICS FOR STRUCTURAL FAILURE PROGNOSIS AND DIAGNOSIS				5a. CONTRACT NUMBER F33615-01-C-5227	
				5b. GRANT NUMBER	
				5c. PROGRAM ELEMENT NUMBER 62712E	
6. AUTHOR(S) Donald A. Shockey Jeffrey W. Simons Takao Kobayashi Dennis Grishin				5d. PROJECT NUMBER L514	
				5e. TASK NUMBER 01	
				5f. WORK UNIT NUMBER 01	
7. PERFORMING ORGANIZATION NAME(S) AND ADDRESS(ES) SRI International 333 Ravenswood Avenue Menlo Park, CA 94025				8. PERFORMING ORGANIZATION REPORT NUMBER SRI Project P11345	
9. SPONSORING/MONITORING AGENCY NAME(S) AND ADDRESS(ES) Materials and Manufacturing Directorate Air Force Research Laboratory Air Force Materiel Command Wright-Patterson AFB, OH 45433-7750				10. SPONSORING/MONITORING AGENCY ACRONYM(S) AFRL/MLLM	
				11. SPONSORING/MONITORING AGENCY REPORT NUMBER(S) AFRL-ML-WP-TR-2004-4232	
12. DISTRIBUTION/AVAILABILITY STATEMENT Approved for public release; release is unlimited.					
13. SUPPLEMENTARY NOTES Report contains color.					
14. ABSTRACT The physics of microstructural deformation and failure in IN100 was investigated to improve existing tools for predicting and analyzing turbine disc failure. A finite element failure model of damage evolution under cyclic loads was developed and applied to simulate fatigue cracking in a compact tension specimen. A procedure was developed for determining from a fracture surface whether a failed component had experienced overloads and for estimating the overload magnitude and crack delay. A method for extracting and categorizing fracture surface features was developed to assist microstructure-based prognosis models and enable a data base approach for failure analysis.					
15. SUBJECT TERMS Failure prognosis, failure diagnosis, microstructural deformation model, fractography, FRASTA, fatigue crack growth, overload effects					
16. SECURITY CLASSIFICATION OF:			17. LIMITATION OF ABSTRACT: SAR	18. NUMBER OF PAGES 50	19a. NAME OF RESPONSIBLE PERSON (Monitor) Jay Jira 19b. TELEPHONE NUMBER (Include Area Code) (937) 255-1358
a. REPORT Unclassified	b. ABSTRACT Unclassified	c. THIS PAGE Unclassified			

TABLE OF CONTENTS

I. Executive Summary	1
II. Introduction and Background	2
Prognosis.....	2
Diagnosis.....	3
III. Finite Element Model of Microstructural Deformation and Failure in IN100	4
Approach.....	4
Crystal Plasticity	4
Test Specimen	6
Explicit Analysis.....	7
Implicit Analysis.....	9
Example Calculation.....	11
Discussion.....	14
Current Status of the Model and Recommendations for Future Work	15
IV. Determining Overloads and Crack Retardation From a Failed Part	16
Background.....	16
Approach.....	18
Test Data	18
Overloads	19
Fracture Surface Topography Analysis	19
Analysis.....	22
Estimating the steady-state plastic strain	25
Evaluation of Models.....	26
Discussion.....	28
Conclusions.....	28
V. Application of Discrete Cosine Transform To Fracture Surface Analysis	29
Background.....	29
The Discrete Fourier and Discrete Cosine Transformations.....	30
DCT Analysis of an SEM image	31
DCT-Analysis of Fracture Surface Topography.....	32
Discussion.....	37
Conclusions.....	39
VI. REFERENCES	39

TABLE OF FIGURES

Figure 1. Polycrystalline structure showing grains and slip planes.	4
Figure 2. Sample stress-strain curve for multi-plane plasticity model.	6
Figure 3. CT specimen.	7
Figure 4. Sample calculation scheme for explicit analysis.	8
Figure 5. Calculation results. (a) damage strain. (b) calculated slip bands. (c) strain-induced cracking at a grain boundary.	9
Figure 6. Finite element mesh of CT specimen for implicit time integration.	10
Figure 7. Details of the finite element mesh in the process zone of the CT specimen.	11
Figure 8. Loading history for CT specimen.	12
Figure 9. Effective stresses in loaded CT specimen.	12
Figure 10. Principal stresses at the grain level around the notch.	13
Figure 11. Calculated plastic strain distribution around growing crack.	14
Figure 12. Crack extension as a function of number of cycles for fatigue tests on IN-100	18
Figure 13. Delay in crack extension due to overload.	19
Figure 14. Fracture surface showing features for crack length measurement at overload applications.	20
Figure 15. FRASTA procedure for reconstructing crack propagation.	21
Figure 16. Relationship between plastic strains below the fracture surface and conjugate topograph displacement in FRASTA.	22
Figure 17. CTD as a function of location on the fracture surface.	23
Figure 18. Deviation in CTD as a function of distance from overload.	24
Figure 19. Relationship between delay in crack growth due to overload and peak deviation.	25
Figure 20. Estimate of steady-state plastic strain.	26
Figure 21. Crack extension as a function of cycles for Specimen 213@20 Hz.	27
Figure 22. Crack extension as a function of cycles for Specimen 213@0.167 Hz.	27
Figure 23. SEM image of fatigue fracture surface of nickel-based superalloy tested at 650 °C. .	31
Figure 24. Reconstructed image using different frequency components.	32
Figure 25. Gray-scale topography image of fatigue fracture surface of titanium alloy.	33
Figure 26. One-dimensional surface topographs.	34
Figure 27. DCT transform of surface profiles.	35
Figure 28. Weighted DCT Amplitude	36
Figure 29. Original topograph image and areas of low, intermediate, and high local surface roughness.	38

I. EXECUTIVE SUMMARY

Fracture physics based tools for predicting and diagnosing structural failure are needed to improve the readiness of DoD assets. The research effort reported here is aimed at improving understanding of the evolution of deformation and failure of material microstructure—an underlying component of practical tools for predicting the fitness of a structural system for the next mission and determining the cause and reconstructing the history of structural failure.

In this project we performed the following:

- (1) Extended the development of a finite element microstructural failure model to simulate damage development in the microstructure of a nickel superalloy. The algorithm can be used in conjunction with continuum/empirical procedures in seeking more accurate predictions of crack growth.
- (2) Developed and demonstrated a procedure for determining from the fracture surface whether a failed component had experienced overloads, and for estimating the overload magnitude and crack delay. This procedure can be used to help determine the cause and history of a failure.
- (3) Developed a method to extract and categorize fracture surface features that will assist in the development of prognosis models and enable a database approach for failure analysis.

The results of this project contribute to the fracture physics base upon which future prognosis and failure analysis technologies will be anchored.

II. INTRODUCTION AND BACKGROUND

The Department of Defense has a recognized need for improved prognosis algorithms and failure analysis tools. Structural failures in aircraft, ships, and other DoD systems cost several billion dollars annually and seriously compromise defense system readiness [1]. For example, in the past decade, failures of aircraft engine components due to high cycle fatigue have resulted in 70 lost fighter planes 23 lost lives, and periodic grounding of the fleet for up to 30 days at a time. The annual costs of lost aircraft, unscheduled maintenance, and component redesign attributed to high cycle fatigue alone is \$600 million. The value of being in a readiness posture in the field cannot be measured in dollars. If a recurring failure mode such as high cycle fatigue could be accurately predicted, or if details of the load history experienced by a failed engine component could be determined, the costs and losses could be substantially reduced by redesigns, altering operational protocols, and choosing alternative solutions such as adding damping or redirecting air flow.

Prognosis

Current methods for predicting structural asset failure (prognosis) are based on continuum assumptions and empiricism. Linear elastic fracture mechanics concepts modified to account for plastic flow are the starting point for most algorithms that attempt to compute crack growth rates and hence component lifetime. Parameters describing material behavior under different load conditions needed for the algorithms are determined by curve-fitting results of failure tests conducted in the laboratory. This approach has served well, but has several important shortcomings. Most particularly, it cannot address the typical wide range of crack growth rates measured in fatigue tests and resulting from the variation in microstructure of real materials. Therefore, failure predictions are modified with large measures of conservatism to ensure failure does not occur. Consequently, the Air Force estimates that over 95% of their turbine engine discs are retired unnecessarily—and at a cost of several hundred million dollars per year.

Continuum/empirical algorithms cannot predict the life of a specific component, because they compute average behavior. The inherent variability of materials and component service history are not considered. Materials exhibit an infinite array of grains, defects, second phase particles, and the like, each of which has different shape, orientation, internal structure, and such, and hence behaves differently when approached by a crack front. This accounts for the scatter band observed in results of a fatigue test series.

Similarly the service experience of a component varies from aircraft to aircraft, and so “identical” components on different aircraft will fail at different times. Differences in the number and severity of maneuvers, foreign object impacts, hot starts, oil starvation, and the like will cause the life of one component to differ from another. Such differences are not accounted for by current life prediction methodologies and thus limit their usefulness in assessing the readiness of a specific asset. Thus, to insure against failure, components are designed and their service monitored using a safety factor applied to the lower bound of the scatter band. As a consequence, components that have substantial life remaining are taken out of service – and at a high cost to the government. A methodology that acknowledges specific mission history and treats microstructure by accounting for deformation and failure occurring at the grain level is needed to circumvent the shortcomings of current life prediction algorithms.

Diagnosis

The inverse of the prognosis problem is failure diagnosis. When aircraft turbine blades and discs fail, details of the cause and progression of damage (often fatigue crack nucleation and growth) need to be determined to prevent future catastrophic failures. At present this desirable information is usually unobtainable. Advances in failure analysis tools are needed. Since the topography of fracture surfaces may hold information about the loads that caused and grew the crack as well as the nucleation time and growth history of the crack, methods to quantify and interpret failure surface features must be developed.

A particular diagnosis issue is to determine the load history experienced by a failed engine component. Such information is necessary for improved component design and for specifying component operating conditions for future missions. In-service baseline steady-state load conditions are superimposed with a random spectrum of overloads and underloads of variable amplitude and frequency. Such load perturbations affect crack front geometry, disrupt steady-state fatigue crack growth, and produce markings on the failure surfaces. If these markings could be detected and quantified, the timing and magnitude of overloads might be obtainable from the failure surfaces of the component. However, an understanding of the effects of overload on crack tip deformation is needed, if more than a correlative relationship between overload magnitude and height of the failure surface mark is to be achieved.

Thus, more reliable tools for failure prognosis and diagnosis require an improved understanding of how material microstructure deforms and fails. The work reported here aimed at advancing failure physics and thereby contributing to improved tools for predicting and diagnosing structural failure.

III. FINITE ELEMENT MODEL OF MICROSTRUCTURAL DEFORMATION AND FAILURE IN IN100

The objective of this task was to develop a failure prognostic algorithm for engineering materials based on the evolution of microstructural damage. A finite element constitutive model was developed that simulates the deformation and failure that occurs in the microstructure of nickel alloy IN100 under fatigue loading conditions. The model was implemented into the three-dimensional finite element code, LSDYNA3D [2] and used to simulate crack growth in an IN100 compact tension (CT) specimen under cyclic fatigue loading conditions.

Approach

The approach for calculating damage evolution is based on a multiplane damage model developed at SRI over the past several years and applied to model cracking in several materials including metals, geological materials, concrete, asphalt, and solid propellant [3]. We were guided in model development by observations and data published by Miner [4], Cowles [5], Mercer and Soboyejo [6, 7] and others [8, 9]. To model the microstructure in crystalline metals, like IN100, each grain in the polycrystalline structure was discretized into computational elements, as shown in Figure 1. Damage accumulates within each element on planes that are oriented along the crystallographic slip planes for that grain.

Within a grain, the planes of all the elements are oriented in the same direction, but for different grains (e.g., grains 1 and 2 in Figure 1), the plane orientations are different. For a polycrystalline structure, the orientation of the planes for each individual grain can be randomly chosen or specified directly, for example, based on data obtained from an orientation-imaging microscope.

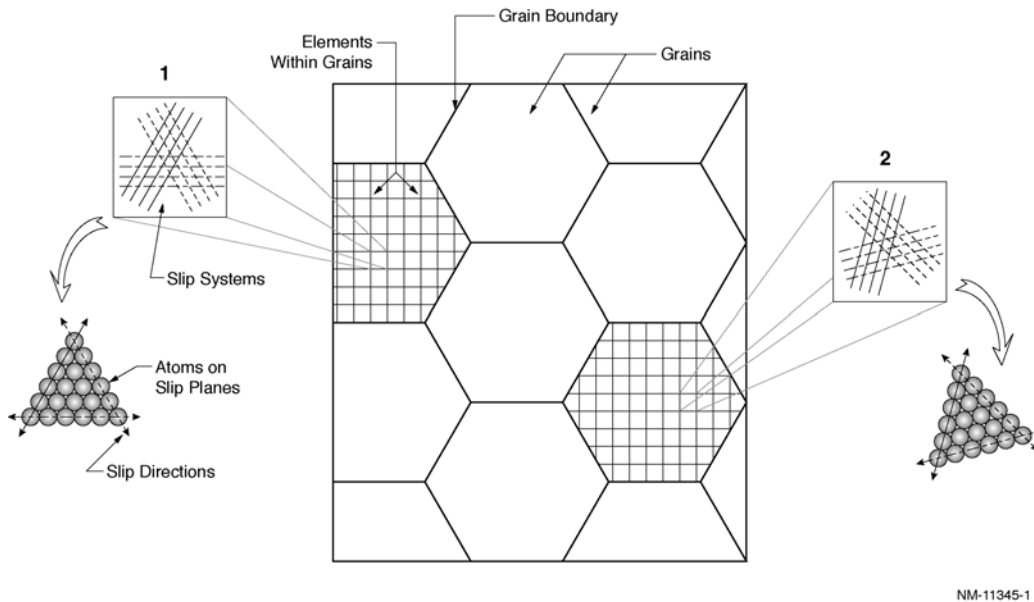


Figure 1. Polycrystalline structure showing grains and slip planes.

Crystal Plasticity

The procedure for calculating the stresses in each element is based on a multiplane compliance method as referenced above. As slip occurs, it increases the compliance of the element in the

direction of shear along the slip plane. To illustrate the computational approach, we describe the procedure for an element with a single slip plane under an applied stress, σ . The total strain, ε^t , in the element is decomposed into elastic, ε^e , and plastic, ε^p , components according to equation (1).

$$\varepsilon^t = \varepsilon^e + \varepsilon^p \quad \text{eq. 1}$$

Plastic strain occurs only on slip planes and in directions corresponding to crystallographic slip systems. As shown in (2), the plastic strain on a plane is calculated from the resolved shear stress in the slip direction through a compliance term, C^p , that includes the transformation of the applied stress into the shear and normal stress components on the plane. In our current formulation, the compliance term is proportional to the current value of slip on the plane.

$$\varepsilon^p = C^p \sigma \quad \text{eq. 2}$$

As shown in (3), combining the compliance due to the plastic strain on the slip plane with the elastic compliance of the element gives an equation for the total strain in terms of σ .

$$\varepsilon^t = C^e \sigma + C^p \sigma \quad \text{eq. 3}$$

Taking the rate form of (3), using the chain rule and rearranging, we can calculate the stress rate in the element from the strain rate for each time step, as shown in Equation (4).

$$\dot{\varepsilon}^t = (C^e + C^p) \dot{\sigma} + \dot{C}^p \sigma \quad \text{eq. 4}$$

Note that C^p changes with time as plastic slip grows, but the elastic compliance, C^e , does not change. In discrete form, as required by the finite element formulation, the increment in stress is given in (5) as a function of the strain increment.

$$\Delta \sigma = (C^e + C^p)^{-1} (\Delta \varepsilon^t - \Delta C^p \sigma) \quad \text{eq. 5}$$

For multiple planes, the compliance of each plane is simply added into the total plastic compliance of the element. Modeling the damage accumulation along slip planes allows many important features of fatigue response of metals, including the growth and broadening of shear bands, to be represented in the simulations. This formulation, combined with data on saturation states of stress, allows us to represent important fatigue plasticity phenomena observed in experiments.

Figure 2 shows the stress-strain curve for an element with two active slip planes and kinematic hardening, subjected to three fully reversed loading cycles. The general shape of these curves is based on the modeling work by Morrison and coworkers [10]. In this example, enough strain was imposed for each cycle to generate clearly observable plastic strain, to show the shape of the hardening curve, and to illustrate the Bauschinger effect. Although it is not obvious from this figure, small amounts of slip occur on the planes even at very low stresses and the stress-strain curve is changing gradually at low loads.

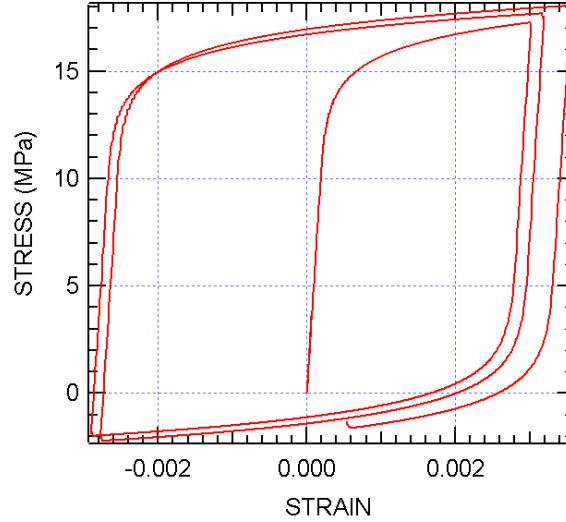


Figure 2. Sample stress-strain curve for multi-plane plasticity model.

The model as such reproduces many of the important features observed in fatigue loading. All shear slip occurs on crystallographic planes and because the effective yield stress is so low, even at stresses well below conventional yield loads, small plastic strains accumulate and form slip bands that grow with many cycles. These growing slip bands interact with grain boundaries and eventually lead to cracking.

We implemented two different approaches for modeling failure of the material. The first method, implemented into the explicit analysis, allows microcracks to initiate by releasing nodes on the grain boundaries when the adjacent elements have accumulated a threshold value of plastic strain. The second method, implemented into the implicit analysis, grows cracks by eroding failed elements. Both formulations allow us to include details about the microstructure into the calculated fatigue response of the material and gives us the capability to implement additional laws governing microstructural damage as more information becomes available.

The constitutive model was implemented as a user-defined material first in DYNA2D and then into LS-DYNA3D. Although the model is formulated to be fully three-dimensional, full three-dimensional analyses of grain structures within a tested specimen are currently not practical on our Linux cluster (8-node PC cluster with 16 Pentium III processors). However, it is practical to analyze full models that are a single element thick.

Test Specimen

As a challenge problem we chose to simulate fatigue tests performed at AFRL. The compact tension (CT) specimen dimensions, shown in Figure 3, are 50.0 mm long, 28.0 mm high, and 9.93 mm thick. The steel loading pins are 10 mm in diameter, spaced at 22.0 mm on center, and located 10.0 mm from the edge. The notch tip is located 17.0 mm from the edge. Two specimens of nickel superalloy IN100 (AS-213, AS-216) were tested at 650°C under well-controlled fatigue loading conditions by workers at the AFRL. Fatigue cracks were grown at a constant baseline maximum stress intensity of 30 MPa $\sqrt{\text{m}}$. The two specimens were tested at different stress ratios, $R=0.05$ for Specimen 213 and 0.50 for Specimen 216, and for each specimen the crack was initially grown at 20 Hz and then at 0.167 Hz. In our simulations, we applied load cycles with

$R=0.05$. Because we did not include dynamic effects or time-dependent effects (such as creep) in the material response, the frequency of loading was not considered.

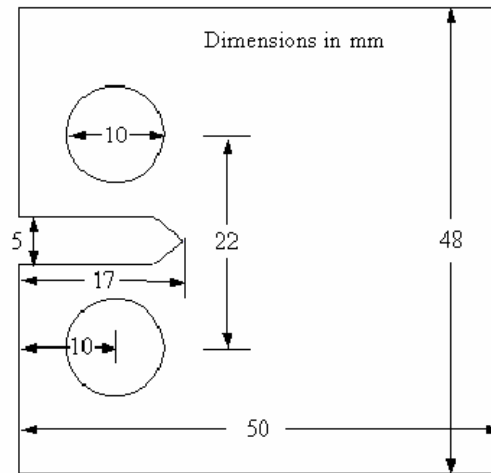


Figure 3. CT specimen.

Explicit Analysis

In the first year we developed the constitutive damage model and analysis method using LSDYNA3D and explicit time integration. To demonstrate the utility of the model we performed a series of simulations to analyze the microstructural response of material in the notch region of the compact tension specimen shown in Figure 3 under cyclic loading. Our approach for the explicit analysis is illustrated in Figure 4. We first calculated the two-dimensional elastic stress field around the notch tip using a relatively coarse mesh. Figure 4a shows the stress contours in the specimen and a closeup view of the mesh at the notch tip. We then created a refined two-dimensional model of the IN 100 microstructure as shown in Figure 4b. At this scale, the mesh consists of gamma grains (shown in colors) interspersed with gamma prime precipitates (shown as gray). The actual grain configuration we modeled was an approximate distribution based on our metallographic observations of IN100, such as shown in Figure 4c. This multiscale method is necessary when explicit time integration is used because the time step required for such small elements makes simulating the whole specimen in a single simulation impractical.

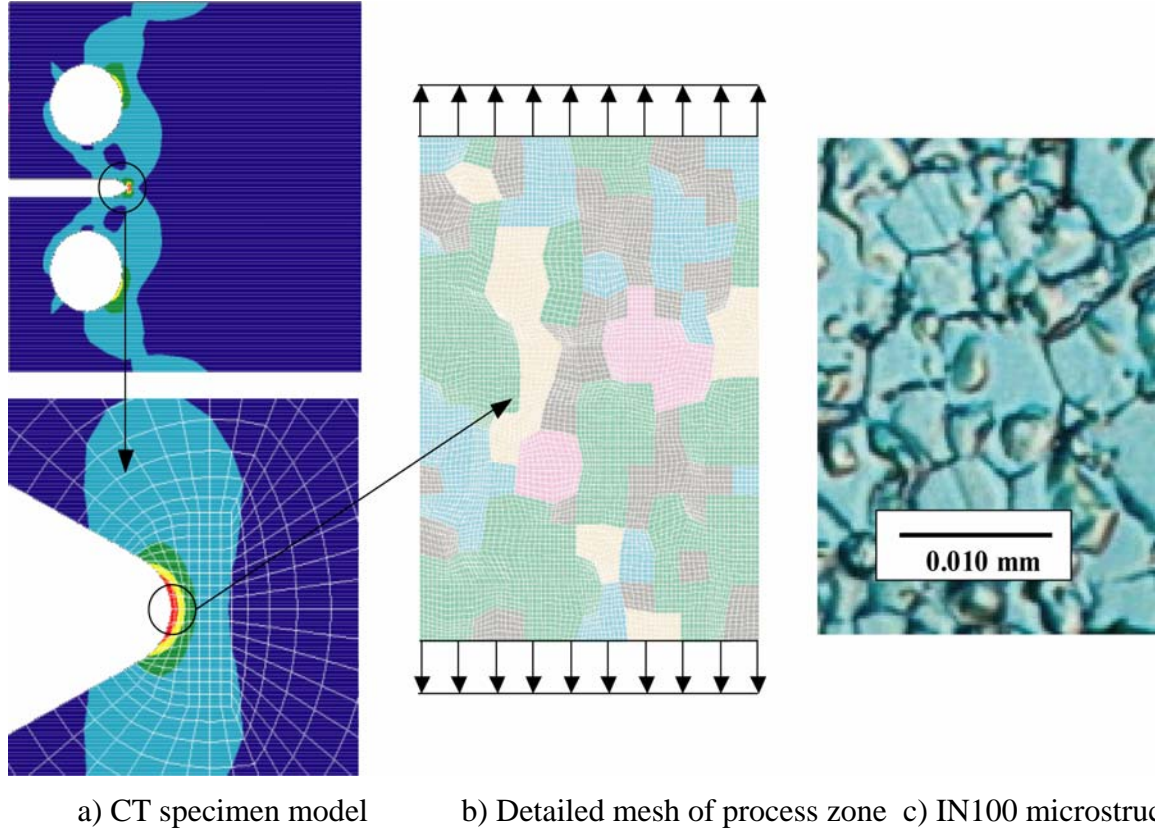


Figure 4. Sample calculation scheme for explicit analysis.

We then applied the stress field for the cyclic load as calculated at the notch tip to the upper and lower boundaries of the refined mesh shown in Figure 4b. The right boundary, along the notch side, was modeled as free, and the left boundary was constrained to move vertically. Details such as slip band growth (length and width), interaction with grain boundaries, and intragranular cracking can be incorporated into the model.

Figure 5 shows fringes of damage strain and calculated slip bands in the microstructure after three fully reversed cycles of above-yield-stress load. Figure 5a shows diagonal bands of high strain in grains that developed as a result of plastic strain occurring on the slip planes. In this image the gamma prime particles, which were assumed to remain elastic, are shown in green. Figure 5b shows that calculated slip bands have grown in the orientations corresponding to high shear stresses in the primary slip directions. The orientations of the slip planes vary among grains because the sets of primary directions for each grain have been given arbitrary initial rotations. Figure 5c shows a highly strained area around a gamma prime precipitate, and an intergranular microcrack that formed because the average plastic strain in the elements at the grain boundaries exceeded the specified threshold limit.

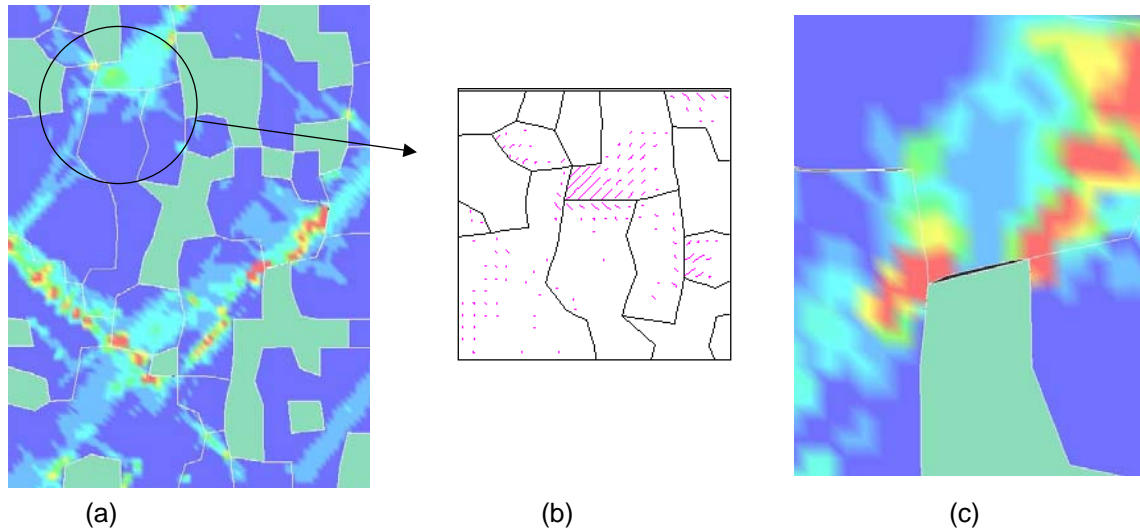


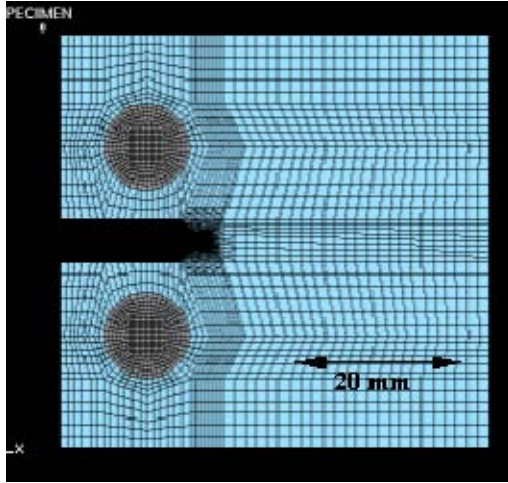
Figure 5. Calculation results. (a) damage strain. (b) calculated slip bands. (c) strain-induced cracking at a grain boundary.

Implicit Analysis

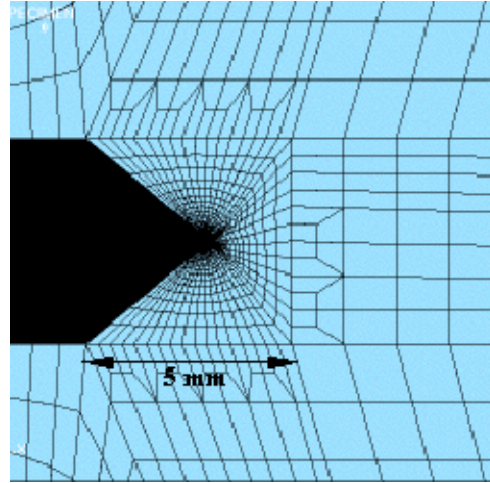
In this second year we improved our finite element model in two significant ways. First, we switched from explicit to implicit analysis which allowed us to model the complete specimen response for several load cycles, and second we improved our model for cracking so that we modeled crack growth through the microstructure.

We began using a new version of LSDYNA3D (Version 970) [2] that includes an option for implicit time integration as well as user defined materials with failure for a Linux platform. Using implicit time integration allows us to calculate fatigue response for an entire CT specimen or disc portion under many cycles of load. Modeling the complete specimen assures correct boundary conditions in the area around the notch tip as damage develops and, at the same time, allows us to use a highly refined mesh around the crack tip to include details of the microstructure.

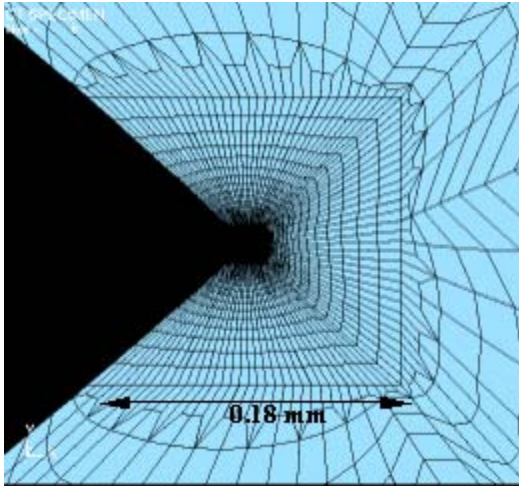
Details of the finite element mesh are shown in Figure 6. Using several levels of transition elements we were able to change the scale of the elements from about 2 mm on a side at the highest level (Figure 6a), down to elements of less than a micron in the process zone. As shown in Figure 6d, at the notch tip, we developed an algorithm that provides a mesh for grains, second phase particles, and grain boundaries, and that maps the grain structure onto a radiused notch.



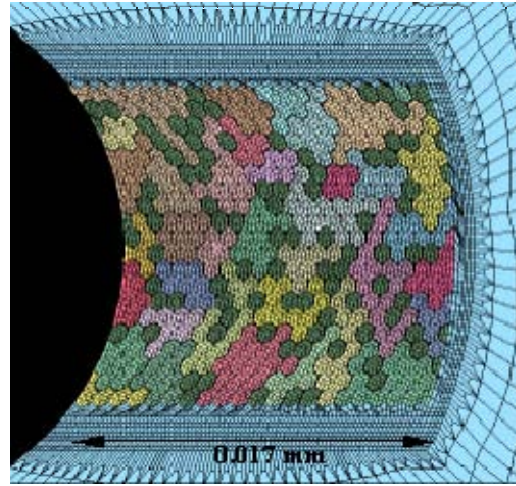
a) CT specimen



b) Notch



d) Notch tip



e) Grain structure around process zone

Figure 6. Finite element mesh of CT specimen for implicit time integration.

Details of the mesh structure within the process zone are shown in Figure 7. Figure 7a gives a representative microstructure for IN100, clearly showing the grain and gamma prime particles. As shown in Figure 7b, the computational grain model for the microstructure is built up using hexagonal blocks, which gives great flexibility in modeling the details of the microstructure geometry. The small green parts represent second phase gamma prime particles, and the alpha grains are shown in other colors.

We developed an algorithm to “grow” a representative grain structure using hexagonal building blocks, in which each hexagon is identified as belonging to a grain or gamma prime particle in a random way within specified constraints. The algorithm starts at one hexagon location and then, using a random number generator, determines whether neighboring hexes are continuations of the current grain (or gamma prime particle), a new grain, or a new gamma prime particle. The algorithm bases the choice on user-specified parameters such as the size of each hexagon (here 3 microns), the average size of a grain and a gamma prime particle, and the ratio of grains and gamma prime particles (in terms of surface area).

As shown in Figure 7c each hexagon is meshed into 12 quadrilateral elements. The chosen mesh structure assures that the shapes of all the elements are well conditioned. As shown in Figure 7d, the grain boundaries are modeled explicitly to account for the distinct material and damage behavior of the grain boundaries as compared to the response of material within the grains.

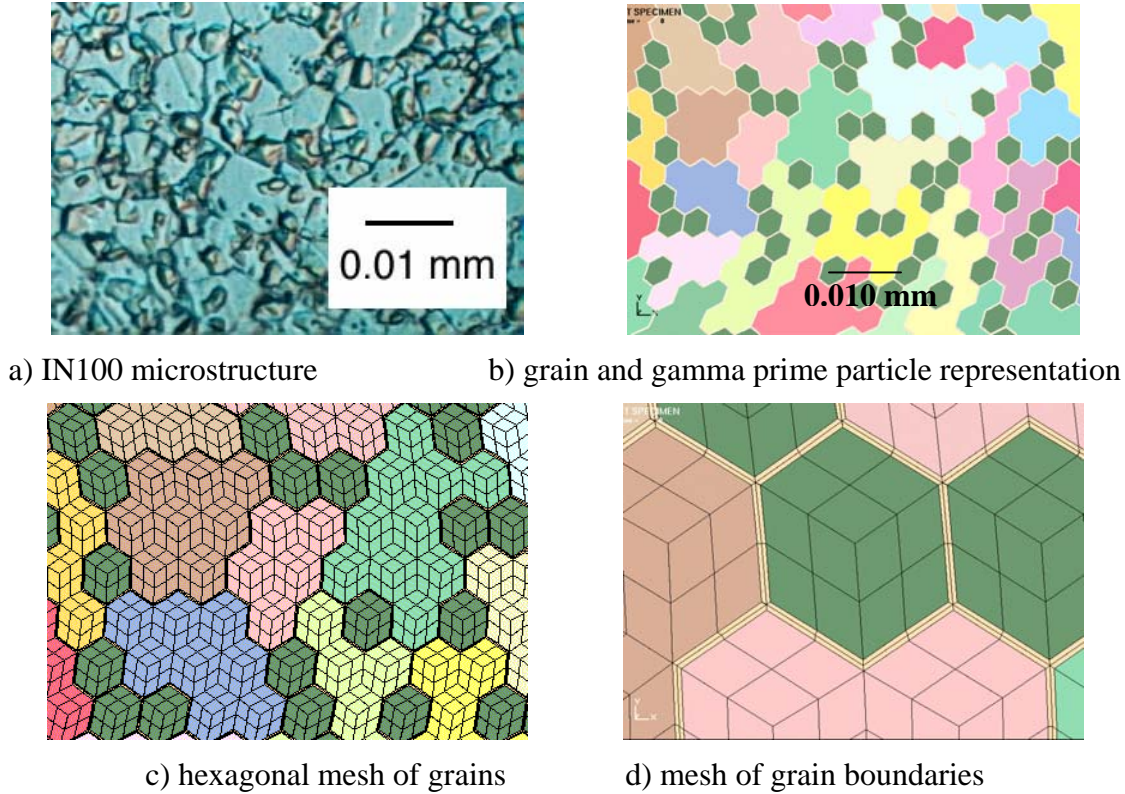


Figure 7. Details of the finite element mesh in the process zone of the CT specimen.

Example Calculation

To demonstrate the model, we calculated damage evolution and fatigue crack growth in the process zone of a cyclically loaded IN100 CT specimen, shown in Figure 6. The loading was applied by specifying a displacement history for the two loading pins, as shown in Figure 8, for the first 7 cycles with a load ratio (minimum load/maximum load) R , of 0.05.

For implicit time integration, the choice of time step is not nearly as restricted as for explicit time integration. In fact, we can perform a loading cycle in relatively few steps (e.g., 6 steps). Because the time step for explicit integration is based on the sound speed across the smallest element (on the order of a nanosecond for a 5 micron element), to calculate several cycles of fatigue response for the entire specimen using explicit integration would take too long to be practical. For this example, using implicit time integration, the model contained about 30,000 elements and each cycle took about 10 minutes of CPU time using a single 2-processor node on our Linux cluster.

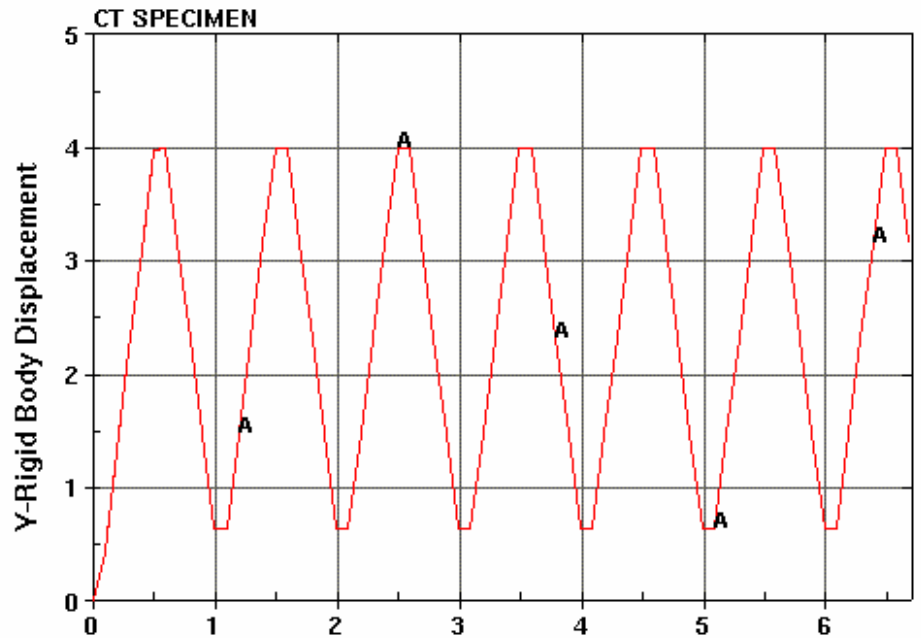


Figure 8. Loading history for CT specimen

Figure 9 shows overall effective stress contours in the CT specimen under peak load. High tensile stress concentrations are evident at the notch, and high compressive stresses are present at the loading pins. The applied displacements (± 0.40 mm at the pins) were chosen to give a maximum load about equal to the baseline stress intensity of $30 \text{ MPa}\sqrt{\text{m}}$.

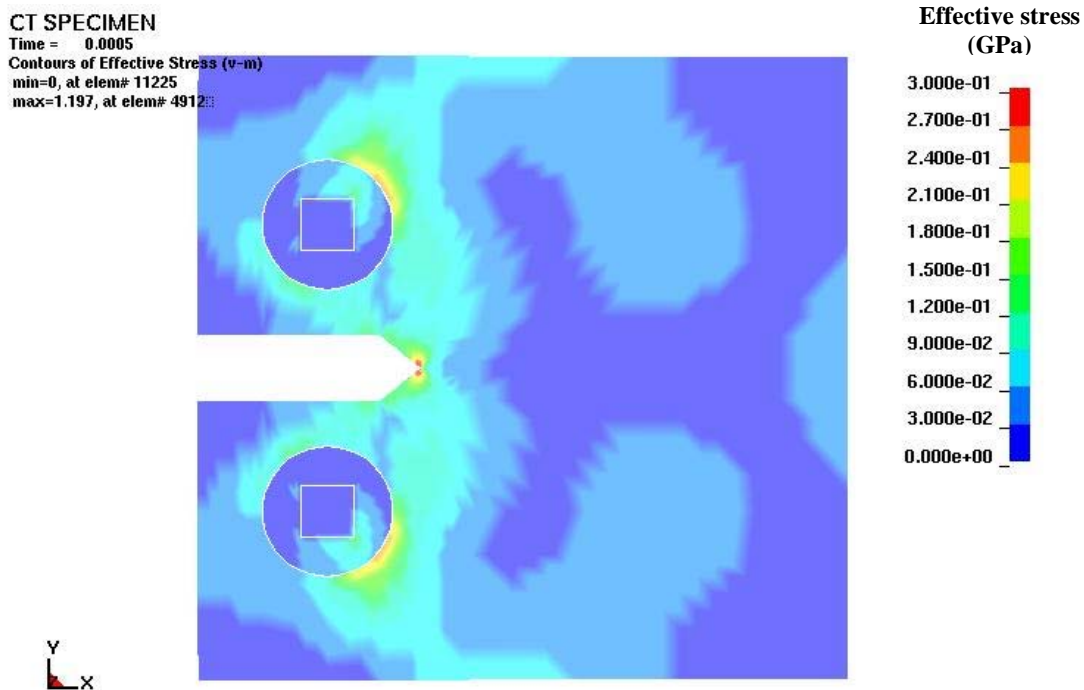


Figure 9. Effective stresses in loaded CT specimen.

The maximum principal stresses in the grain structure at the notch tip are shown in Figure 10. The calculation shows the overall stress gradient at the notch tip that exists across grains in the microstructure. It also shows the nonuniform stress distribution in the grain structure due to the microstructure, in particular “hot spots,” or high stresses that could produce microcracks ahead of the crack front.

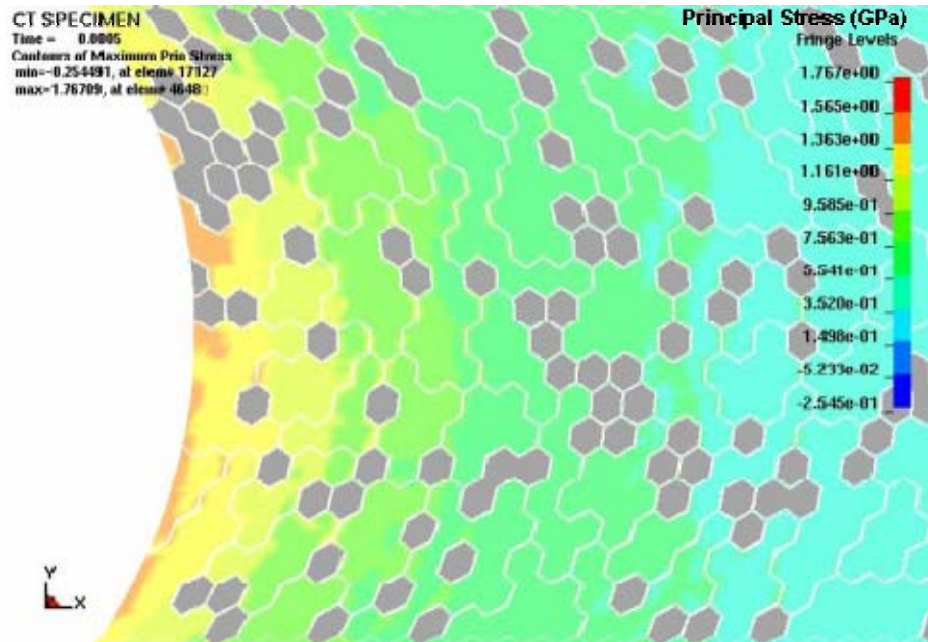


Figure 10. Principal stresses at the grain level around the notch.

Figure 11 shows calculated growth of a crack through the IN100 microstructure under load cycles 4 through 6. Fringes of maximum principal stress are shown, illustrating the stress concentration that accompanies the crack tip as it progresses through the microstructure. Note that the stress distribution varies with location as a result of the differences in microstructure the crack encounters while growing. The crack grows by failing elements at the crack tip. A creep-type failure criterion was used. Failure occurred if the maximum principal stress in an element was above a threshold stress for longer than a specified duration. Note that the crack initiates at several locations, but that only a single crack path develops.

For future reference we note that the plastic strain in the element at the time of the failure affects the topology of the fracture surface. Thus the calculated results are useful in failure diagnostics and in interpreting the results of FRASTA, which is a technique for fracture surface topographic analysis [11, 12].

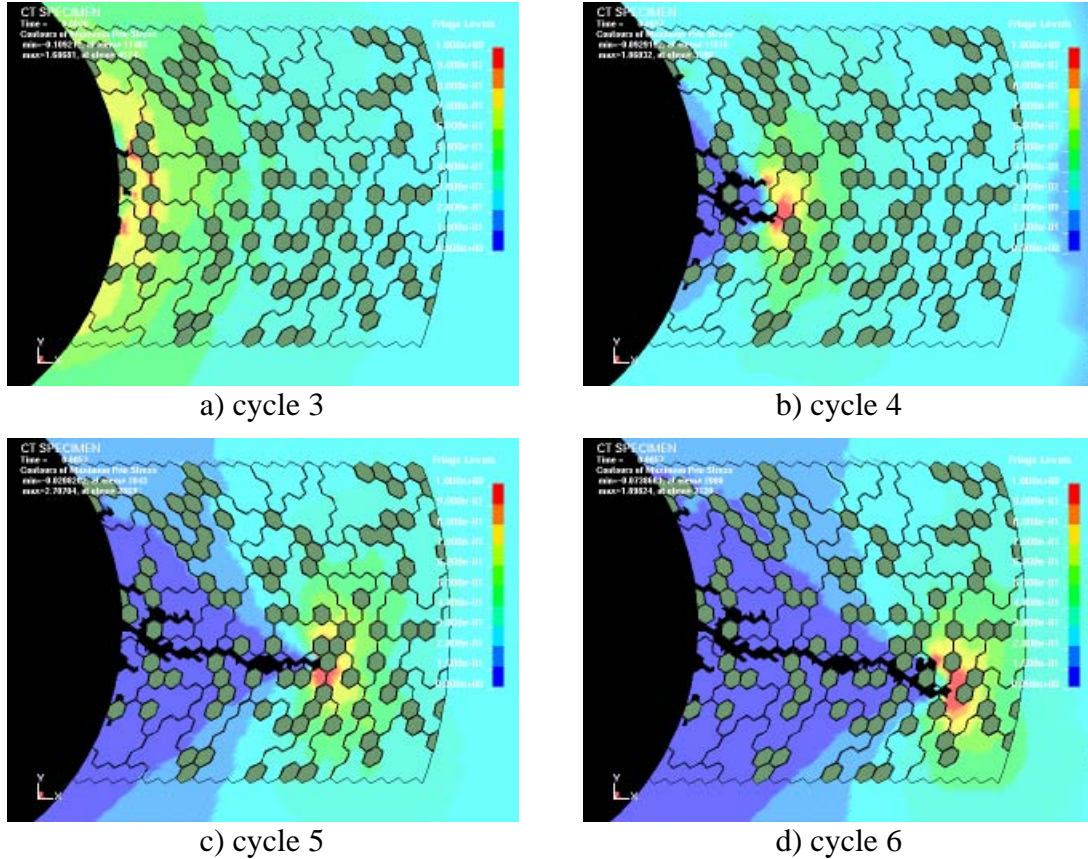


Figure 11. Calculated plastic strain distribution around growing crack.

Discussion

The computer images in Figure 10 depict the details of how stresses and damage evolve in the IN100 microstructure. After three loading cycles, material farther than 40 microns from the notch surface senses no enhanced load, but a band of material beneath the notch surface about 40 microns wide experiences enhanced principal peak stresses of about 0.7 GPa and material within about 10 microns of the notch surface is stressed to 1.2 GPa, Figure 10a. The elevated stresses in the 10-micron band are sufficient to activate slip on favorably oriented crystal planes. The slip bands pile up at grain boundaries and concentrate the stress where they meet. Microcracks appear where the stress concentrations exceed the failure strength.

On the next load cycle several additional microcracks nucleate at the notch surface and a previously nucleated crack bifurcates and extends into the material. Stresses are elevated at the tips of the bifurcated crack, whereas material in the crack wake experience compressive stresses. Material outside the compressive zone is unloaded.

In Cycle 5 the crack branch with the smaller stress at its tip ceases to grow and the other branch propagates as a single crack. Growth is transgranular and along gamma prime interfaces. The crack wanders through the microstructure seeking the path of least resistance, i.e., grains oriented such that weak crystal planes and grain boundaries are nearly perpendicular to the tensile stress direction.

The failure surface resulting from the wandering crack consists of the exposed surfaces of grains that have been traversed by the crack and those whose boundaries have failed. Deformation preceding grain failure is also manifested on the surface. The amount and character of this deformation is dependent on the loads, and hence provides a route for failure analysts to deduce the load conditions that caused a component to fail. The FRASTA technique, which compares the topography of conjugate fracture surfaces, attempts to measure this deformation and extract the causative load conditions.

Thus, the results of the model are qualitatively and intuitively in accord with expected evolution of microstructural deformation and failure [4-9]. The results should be compared with observations and data obtained by serial sectioning or focused ion beam examination of cross sections taken through the crack front. Further, the predicted and measured failure surface topography should be compared quantitatively to evaluate the use of the model in failure diagnosis.

Current Status of the Model and Recommendations for Future Work

We have developed and demonstrated a computational model for simulating the evolution of damage and growth of microcracks at a crack front in IN100 under cyclic load. The model shows the feasibility of using advanced finite element modeling techniques to compute fatigue crack growth through a superalloy microstructure.

In its present state the model can be used to investigate the effects of microstructure on crack nucleation and growth. This can be accomplished by performing parameter studies in which aspects of the loading and microstructure of the material are varied. For example, simulations of the Tests 213 and 216 under other combinations of K_{max} , ΔK , stress ratio R , and frequency would indicate their effect on damage evolution and assist in quantifying model parameters.

The CT specimens analyzed previously showed a significant difference in failure mechanism for high and low frequency cyclic fatigue. Under low frequency cycling, fracture was intragranular but under high frequency cycling it was transgranular. We suspect that the difference is due to the occurrence of creep at the grain boundaries during low frequency cycling, which leads to grain boundary failure. In the current model the grain boundaries have the same properties as the grains. We need reference data describing grain boundary response in IN100 to better characterize deformation properties of the material at the grain boundaries, especially with regard to creep properties. We need to model this frequency-dependent response and implement a creep-type material model into the grain boundary elements.

In developing a model for IN100, we used NASA's [13] cyclic stress-strain curves from round bar tests and crack growth rates for CT specimens. The microstructural aspects of the model need to be checked and further developed by including microstructural observations and data. We suggest performing interrupted fatigue experiments, in which microstructural and loading parameters are varied. The specimens should be assessed metallographically to check the fidelity of the computations and to acquire insight and data for model refinement. The data should include slip band dimensions and details of topographic features on fracture surfaces.

IV. DETERMINING OVERLOADS AND CRACK RETARDATION FROM A FAILED PART

Fatigue failure surfaces were produced in nickel alloy IN100 under steady-state cyclic load conditions and isolated overloads of magnitudes up to 1.75 times the baseline stress intensity. Fracture surface topographies at the overload sites were measured by confocal microscopy and analyzed by FRASTA to determine the size and shape of the plastic crack opening stretch (COS). The deviation from the linear relation between crack length and COS indicated the overload magnitude and crack delay, showing that load conditions and crack histories can be deduced from a failed part.

Background

Fatigue of aircraft components is a major DoD problem, resulting in large annual costs and sporadic fleet groundings. [1] When a component fails, details of the crack nucleation and extension are sought so that the component can be redesigned or operation, inspection, and maintenance protocols can be adjusted to reduce the likelihood of future failures.

If crack history could be reliably monitored or predicted, cracked components could be taken out of service before they failed. Under steady-state cyclic loads, crack growth rate is constant. But the baseline steady-state cyclic load conditions of many aircraft components are superimposed with a random spectrum of overloads and underloads of variable amplitude and frequency, and these can strongly disrupt steady-state crack growth. [13, 14] Thus, a turbine disc may fail before the end of its expected mission life, because the overload spectrum experienced by the disc was unknown and therefore not accounted for in the fracture mechanics models used to predict life.

This situation could be improved if a way existed to determine the spectrum of overloads experienced by a component during service. But this is often difficult. Pilot reports are usually qualitative and often unreliable, and on-board sensors generally do not provide information close enough to the failure to be useful. In many instances the failure analyst must attempt to extract the operative loads and crack history from the failed part.

Here fracture surfaces are invariably turned to in seeking the critical information. An overload should stretch material at a fatigue crack front, blunt the front, and leave a mark on the fracture surface after the crack advances. Moreover, the extent of crack front stretching should be proportional to the overload magnitude. Thus, if markings could be observed and measured, it may be possible to assess the number, sequence, and magnitudes of overloads from examination of a failed part.

A number of researchers have attempted to extract load information from fracture surfaces. Murakami, Furukawa and their colleagues [15, 16] microtomed fatigue fracture surfaces of an aluminum and two steel alloys and found a relationship between the stress ratio, R , and the ratio of striation height and spacing. This relationship, when combined with striation spacing versus ΔK data, permits determination of the maximum and minimum stresses of the cyclic load spectrum. Kaneko et al. [17] applied a 3D scanning electron microscopy (SEM) technique to quantify fracture surface roughness of a nickel alloy and correlated the result with vibratory stress. They also used electric backscattering patterns to measure the depth of the plastic zone beneath the fracture surface and correlated it with K_{max} . They claim an accuracy of $\pm 25\%$.

Ranganathan and coworkers [18] identified facets, striations, and dimples as salient features on fracture surfaces of three aluminum alloys and developed a grid technique to quantify their

spatial distributions. Plots of percent area of the feature versus load parameters showed that peak to peak load ratio and maximum stress intensity factor are most important in determining fracture surface appearance. The authors proposed a fractographic technique for determining K_{\max} and R for both block loads and variable amplitude loading.

Varvani-Farabani [19] and Kardomateas [20] considered the plastic crushing of fracture surface asperities as a measure of stress ratio, R . The height of surface irregularities as measured with confocal laser microscopy in [19] decreased linearly with increasing compressive overloads, resulting in reduced crack closure and increased crack growth rate, and pointing to a way to estimate loads via fractography. Compression-induced abrasion marks were evident when examined with SEM. A micromechanical crushing model of crack face asperities [20] predicts load ratio, R , from fracture surface roughness.

Other workers have attempted to determine material properties fractographically [21, 22, 23, 24]. The blunting that occurs at the tip of a fatigue precrack when a fracture toughness specimen is loaded to failure manifests itself on the fracture surfaces, producing a stretch zone with clear boundaries, namely a distinct width (stretch zone width, SZW) and height (stretch zone height, SZH). Stretch zone dimensions have been measured with profilometry, stereo techniques, and Moiré interferometry, and a relationship has been found between SZW and SZH and the crack tip opening displacement, and hence, the fracture toughness of the material. It has been suggested that stretch dimension measurement is a method to determine fracture toughness of materials. A number of researchers have published data for ductile materials such as Armco iron, pure copper, etc., that support the suggestion.

The success in determining fracture toughness fractographically suggests that overload magnitudes might be obtained from the fracture surfaces. Subcritical stretch zones will result from loads insufficient to cause failure, and the height will vary according to the overload. Thus, when an overload is applied to a specimen or component containing a fatigue crack during cyclic loading, the crack tip is blunted, and if the stretch zone height can be measured, a quantitative estimate of the overload might be obtained.

However, it is not sufficient to measure the SZH on one surface only and then double the result. Krasowsky [25, 26] and his colleagues showed clearly that the stretch height is not symmetrically divided on the two fracture surfaces. Because the crack usually grows from the blunted zone at an angle to the nominal fracture plane, the deformation left on one of the surfaces may be quite different on the other. Therefore, in attempting to extract overload magnitude fractographically, the SZH on the mating surfaces must be measured and added.

The goal of this work was to develop a method for detecting overload markings on fatigue failure surfaces and for estimating overload magnitudes. We applied a technique for quantifying and analyzing failure surface topography to nickel-alloy compact tension specimens tested under well-controlled fatigue conditions with systematic overloads.

Approach

Test Data

Two compact tension specimens of nickel superalloy IN-100 (AS-213, AS-216) were tested at 650°C under well-controlled fatigue loading conditions by workers at the AFRL. Fatigue cracks were grown at a constant baseline maximum stress intensity of 30 MPa√m. The two specimens were tested at different stress ratios, $R=0.05$ for Specimen 213 and 0.50 for Specimen 216, and for each specimen the crack was initially grown at 20 Hz and then at 0.167 Hz. For each set of conditions, overloads of three different magnitudes (37.5, 45, and 52.5 MPa√m) were applied, separated by several millimeters of crack growth, so that effects of individual overloads could be determined.

Crack front location measured by the DC electric potential (DCEP) drop technique is plotted as a function of loading cycles in Figure 12.

Table 1 lists the steady-state crack growth rates for the four different sets of conditions. The crack grows about three times faster for $R=0.05$ ($\Delta K=28.5$ MPa√m) than for $R=0.5$ ($\Delta K=15$ MPa√m) and four to five times faster at 0.167 Hz than at 20 Hz.

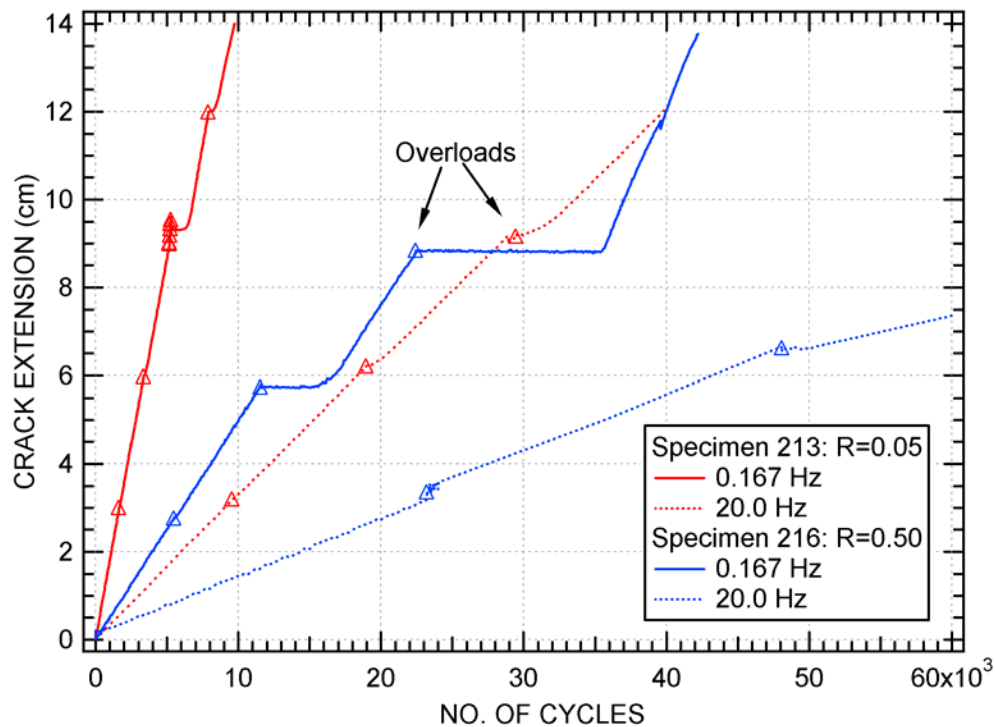


Figure 12. Crack extension as a function of number of cycles for fatigue tests on IN-100

Table 1. Steady-state crack growth rates

K_{\max}	K_{\min}	Stress Ratio	Frequency (Hz)	da/dN ($\mu\text{m}/\text{cycle}$)
30	1.5	0.05	0.167	1.80
30	1.5	0.05	20.0	0.328
30	15	0.50	0.167	0.503
30	15	0.50	20.0	0.131

Overloads

The disruptive effect of an overload can be seen by examining fatigue crack length as a function of the number of cycles. Figure 13 shows the relationship for the third overload (52.5 MPa $\sqrt{\text{m}}$ at cycle 29434) on the section of Specimen 213 tested at 20 Hz. In the region before the overload this curve is linear; i.e., the crack velocity is constant at about 0.33 $\mu\text{m}/\text{cycle}$. At the site of the overload, the velocity decreases significantly, then slowly increases until, about 2000 cycles after the overload, the crack again grows at the initial velocity. By comparing the initial and final curves we can assess the delay in the crack growth due to the overload in terms of cycles (about 1600 cycles) or crack extension (about 400 μm).

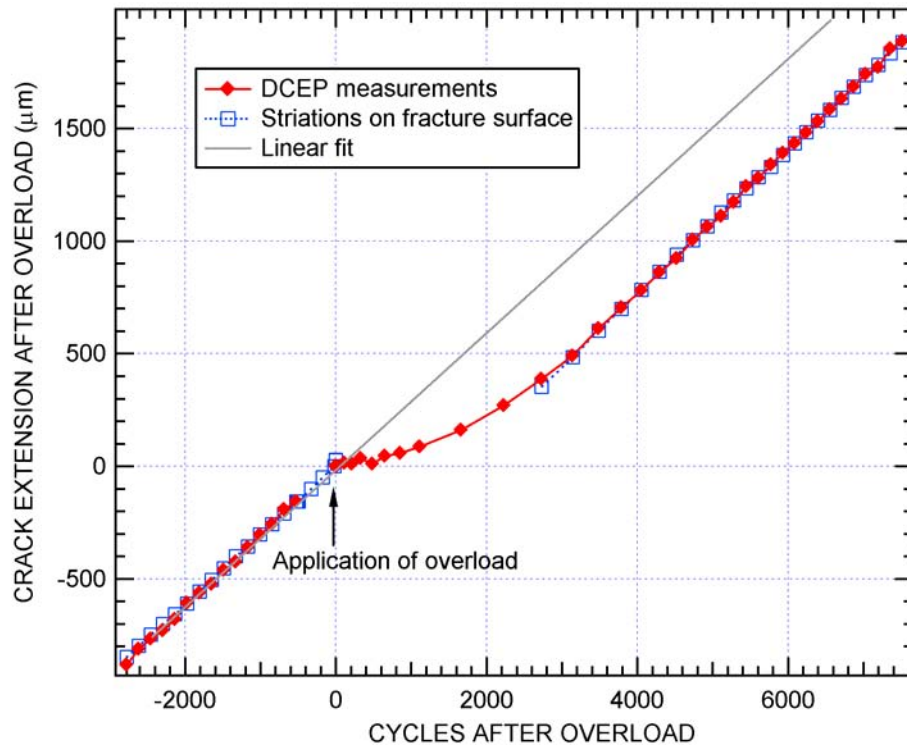


Figure 13. Delay in crack extension due to overload

Fracture Surface Topography Analysis

Figure 14 shows a portion of the fracture surface for IN100 tested at $R=0.05$ and 20 Hz. The striations on the surface were produced by the DCEP procedure used to measure the crack length. During the test, fatigue cycling was slowed to measure the crack length, and the fracture

surface at these locations had different features than that generated by the baseline 20 Hz fatigue cycling. As shown in Figure 13, by measuring the striations and comparing the crack growth rates, we were able to assure confidence in the DCEP measurements.

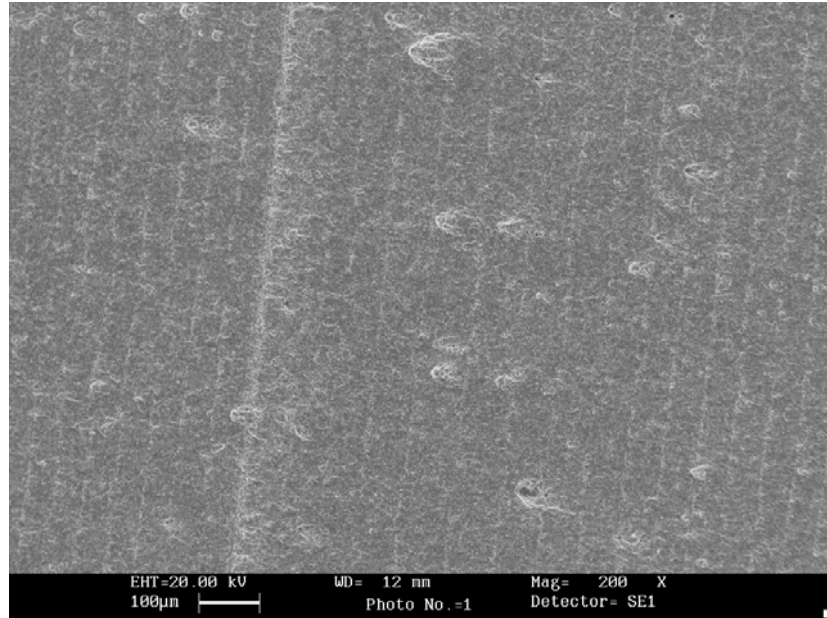
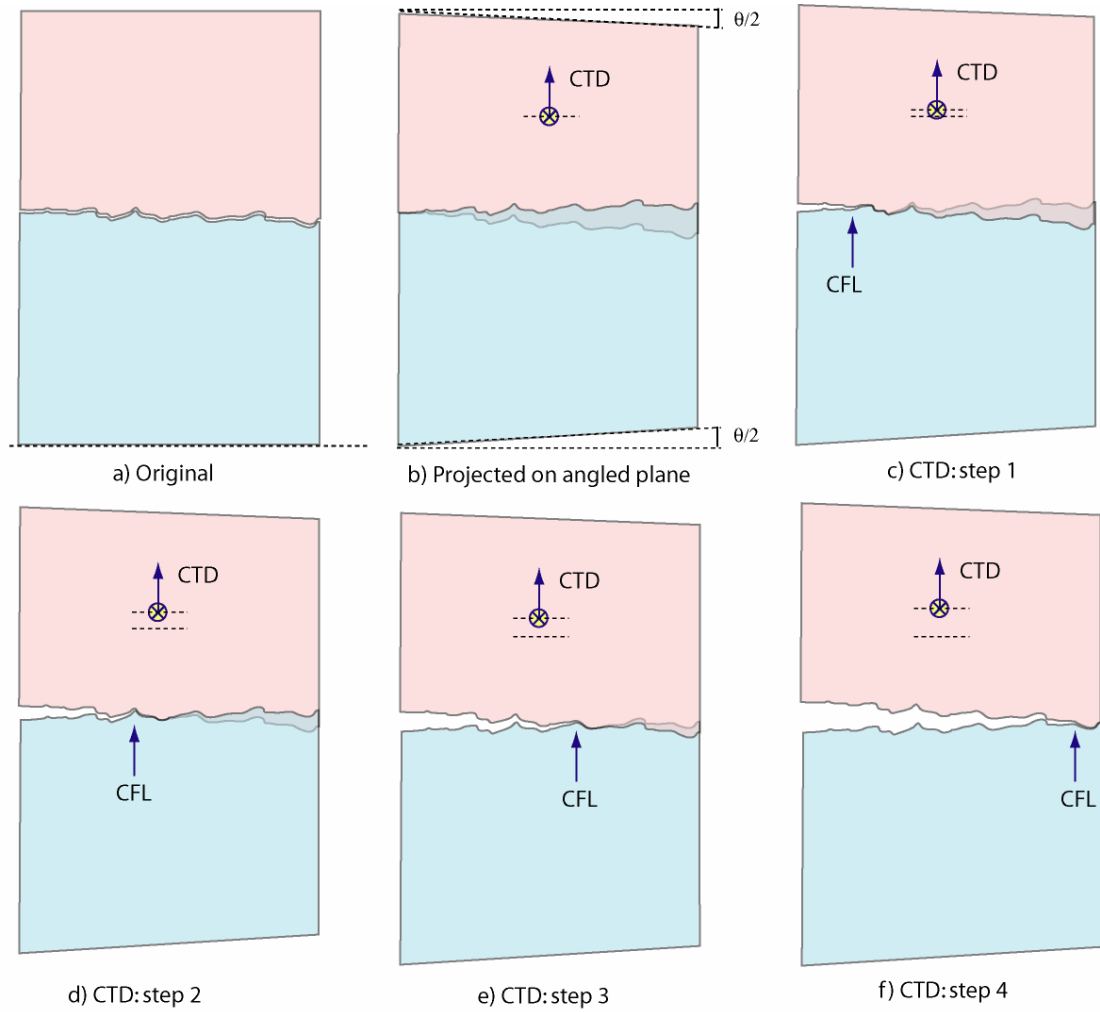


Figure 14. Fracture surface showing features for crack length measurement at overload applications.

The failed specimens were analyzed using FRASTA, a procedure in which topographs of the conjugate fracture surfaces are juxtaposed and positioned relative to each other to simulate the configuration of the crack faces as the crack grows during the fatigue tests (Figure 15). As shown in Figure 15a, topographs created using a scanning laser confocal optics microscope are initially positioned so that the two reference planes are parallel and the fracture surfaces line up. Then, as shown in Figure 15b, the reference planes are rotated by an angle $\theta/2$ and the fracture surfaces are projected onto the rotated planes. The angle θ is typically small (on the order of 1°) and corresponds approximately to the crack opening angle for the baseline loading. As shown in Figure 15c-f, as the upper topograph is displaced upwards, as measured by the conjugate topograph displacement (CTD), the crack apparently grows and the crack front location (CFL), defined as the intersection of the two topographs, moves from left to right.



CTD is Conjugate Topograph Displacement
CFL is Crack Front Location

Figure 15. FRASTA procedure for reconstructing crack propagation.

For two fracture surfaces that line up exactly, for example a crack in a brittle, elastic material, as shown in Figure 16a, the CFL has a linear relationship with the CTD. The slope of the curve, S , as shown in Figure 16, is given by,

$$S = \tan(\theta) \quad \text{eq. 6}$$

Crack surfaces developed under steady-state conditions with plastic deformation at the crack tip have a uniform field of accumulated plastic strain beneath the fracture surface and would produce the same CTD vs. CFL curve. However, under overload conditions, additional plastic strain is developed beneath the crack surfaces in the region around the overload application. This accumulated plastic strain shows up as additional overlap between the fracture surfaces and thus increased CTD is required to advance the crack. The accumulated plasticity appears in the CTD vs. CFL curve (Figure 16) as a deviation from the otherwise straight line. The magnitude of the deviation in terms of CTD is a measure (in μm) of the accumulated plastic strain below the

surfaces (in addition to the steady-state value) due to the overload. Hence the CTD is the increment in crack opening stretch (COS) [27] resulting from the overload.

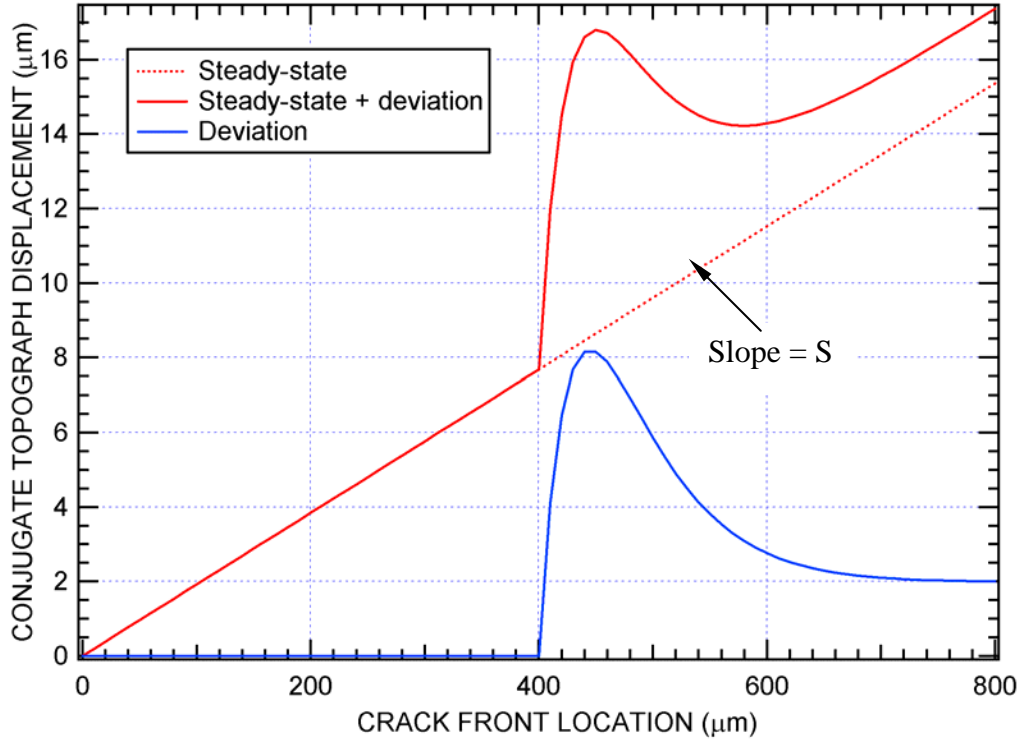


Figure 16. Relationship between plastic strains below the fracture surface and conjugate topograph displacement in FRASTA.

Analysis

For the fracture surface regions around each of the overloads we generated deviation profiles and peak deviations from the CTD vs. CFL curves and correlated these with the overload magnitude. From the crack extension histories, such as that shown in Figure 17, we estimated the effective delay in number of cycles due to the overloads. We were then able to correlate the peak deviation caused by the overload to the effect of the overload in terms of number of cycles delay and investigate the effects of load ratio, R , and cycling frequency on this relationship.

As an example, we illustrate the procedure for the section shown in Figure 14, the third overload ($52.5 \text{ MPa}\sqrt{\text{m}}$ at cycle 29434) on the section of Specimen 213 tested at 20 Hz. Figure 17 shows the CTD vs. CFL curve along with a linear segment fit to the pre-overload section. The location of the overload is at about 400 microns on the CFL. The effect of the overload is clearly visible. At some distance (about 50 μm) before the overload, the curve begins to deviate from the pre-overload section, and then slowly returns to a curve parallel to but offset from the initial line.

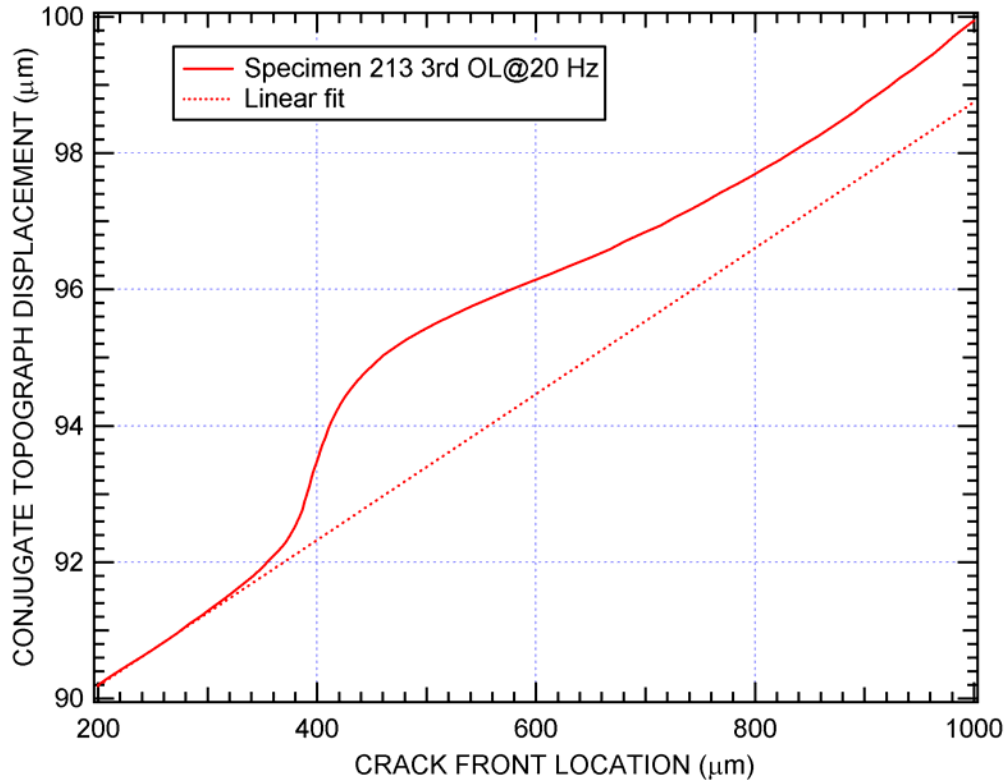


Figure 17. CTD as a function of location on the fracture surface.

As explained above, the deviation from the pre-overload straight line is related to the additional plastic strain in the region beneath the fracture surface around the point of overload application. Figure 18 shows the deviation in CTD as a function of the distance from the overload. This curve has a peak of about 2.2 μm , located about 100 μm beyond the location where the overload was applied. The offset after the curve returns to the initial slope may have contributions from several sources including:

- (1) Changes in steady-state conditions caused by overloads. Because the tests are performed under constant stress intensity, the load is adjusted for the crack length as determined with DCEP. Any error from the overload in determining the crack length would change the steady-state loading conditions and add an offset.
- (2) Problems with resolution in determining the CTD vs. CFL curve
- (3) Uncertainties in setting the slope of the initial line.

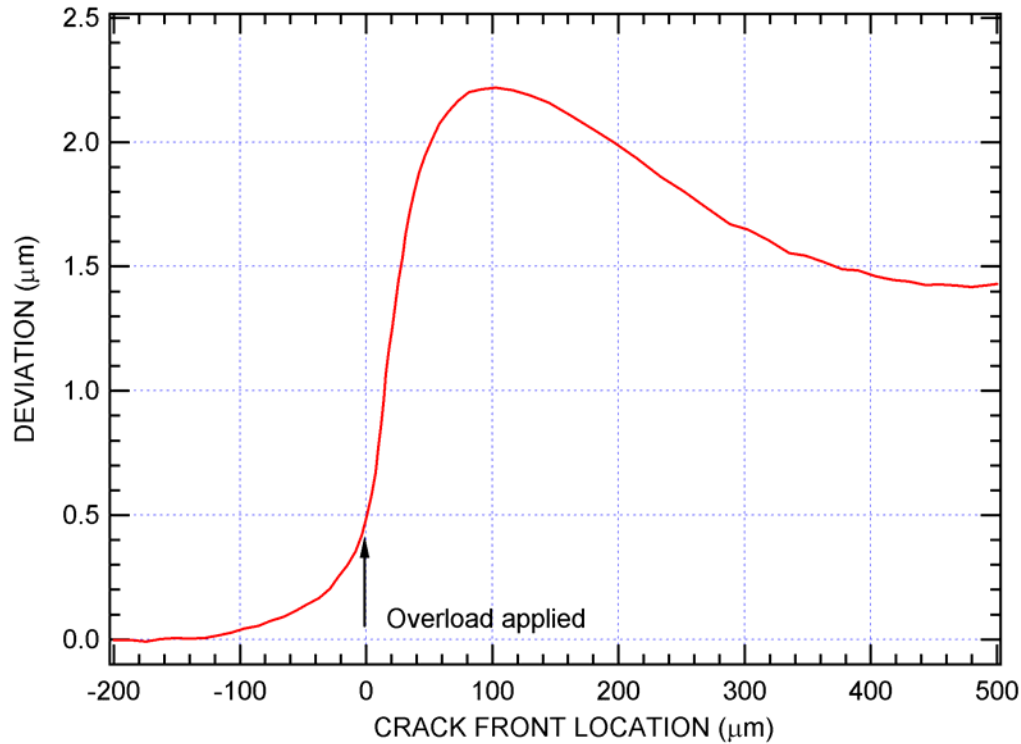


Figure 18. Deviation in CTD as a function of distance from overload.

The peak deviations and the delay in cycles due to the overloads for Specimen 213 ($R=0.05$) are listed in Table 2, and plotted in Figure 19. There is good correlation between the peak deviation and the delay in number of cycles. As the deviation increases, the delay is greater. The two curves for different frequency loading are close to each other. The data point for 7 cycles at 52.5 MPa \sqrt{m} is consistent with the data points for single overload cycles. For Specimen 216, delays in the crack growth were not obtainable for the 20 Hz cycling because of apparent problems in accurately monitoring crack length. The curve for the 0.167 Hz section has the same basic shape, but lies well above the curves for Specimen 213.

Table 2. Peak deviations and delay cycles for IN-100 Specimen 213 ($R=0.05$)

	OL	Peak Dev (μm)	Delay (cycles)
20 Hz	37.5	0.42	145
	45	1.3	566
	52.5	2.2	1655
0.167 Hz	37.5	0.25	35
	45	0.56	151
	52.5	1.1	483
	7@52.5	1.9	1026

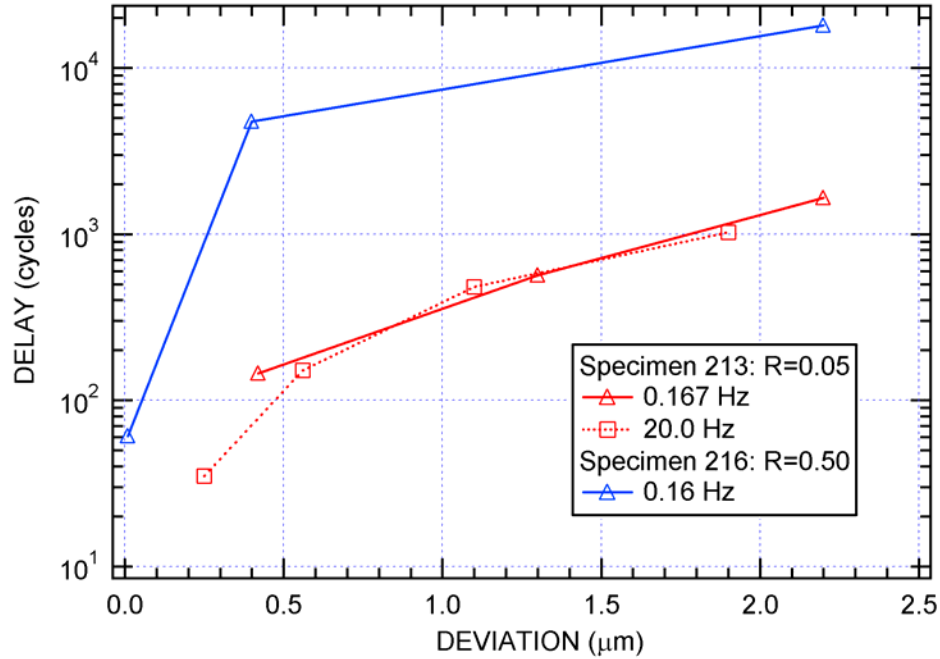


Figure 19. Relationship between delay in crack growth due to overload and peak deviation.

Estimating the steady-state plastic strain

As described above, the deviation of CTD from the steady-state straight line gives plastic strain caused by overloads in addition to that produced during steady state crack growth. Ideally, we would like to have the full value of plastic strain accumulated below the fracture surface. To estimate that value, we constructed the curve shown in Figure 20, which shows peak deviation as a function of overload magnitude. The data points from the experiment are at overload magnitudes of 37.5, 45, and 52.5 MPa√m., but are shifted by an unknown steady-state value at 30 MPa√m. We also know that at 15 MPa√m, IN100 reaches a fatigue limit, i.e., fatigue cracks won't grow. Assuming a value of zero plastic strain at 15 MPa√m, we simply tried steady-state values for deviation at 30 MPa√m and tried to get curves with monotonically varying slopes. Values between 0.4 and 0.7 μm for 20 Hz and 0.2 and 0.4 μm for 0.167 Hz gave reasonable-looking curves.

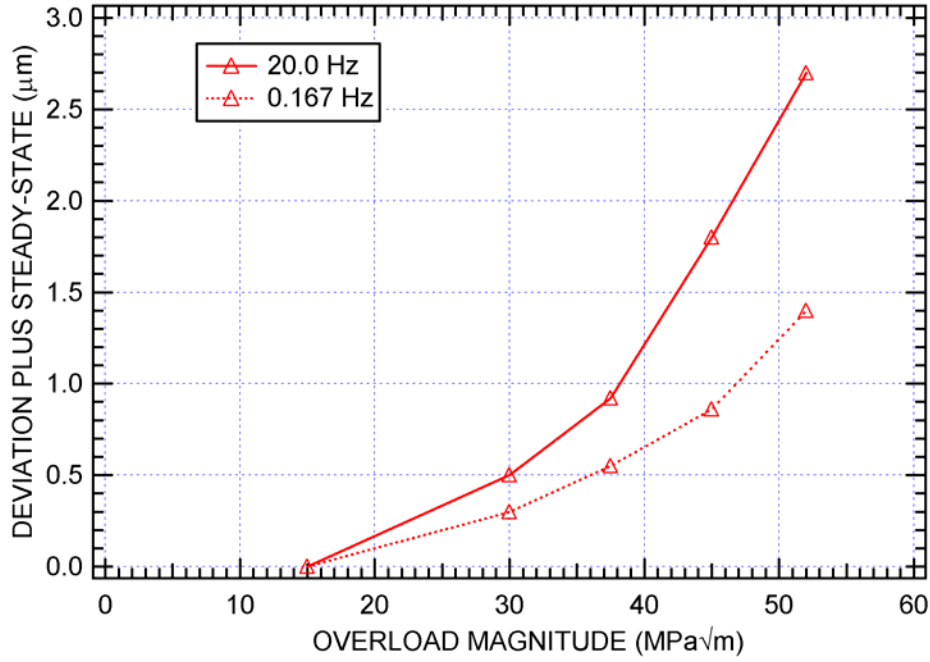


Figure 20. Estimate of steady-state plastic strain.

Evaluation of Models

We compared the measured delays caused by the overloads with the predictions of the formula given by Wheeler, [28]

$$a_r = a_0 + \sum_{i=1}^2 C_{pi} f(\Delta K_i) \quad \text{eq. 7}$$

where a_r is the current crack length, a_0 is the crack length at the time of the overload application and C_{pi} is a retardation parameter given by

$$C_{pi} = \left(\frac{R_y}{a_p - a} \right)^m \quad \text{eq. 8}$$

where R_y is the radius of the yielded zone due to the overload and m is a material parameter. The model was fit to the data with the exponent $m=3.1$ by matching the final offset for crack extension for the 45 MPa√m overload for Specimen 213 at 20 Hz. As shown in Figure 21, the model gives a reasonable estimate of the delay resulting from overloads of 37.5 and 45, but overpredicts the delay for 52.5 MPa√m by almost a factor of two.

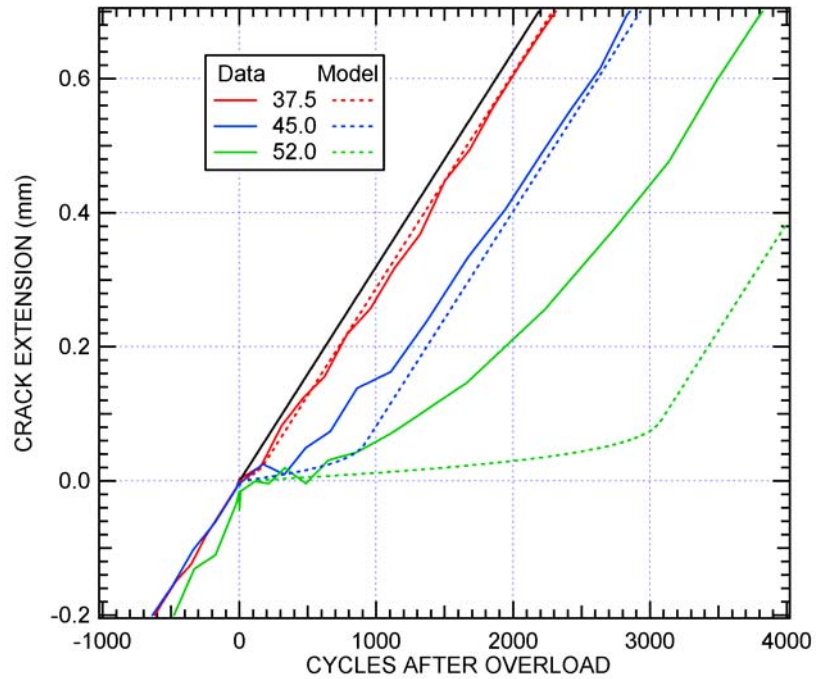


Figure 21. Crack extension as a function of cycles for Specimen 213@20 Hz.

For Specimen 213 tested at 0.167 Hz, the model gives reasonable estimates for all three overloads (Figure 22). The data for 52.5 MPa√m is somewhat suspect because the steady-state velocity for the crack well after the overload is less than that before the overload.

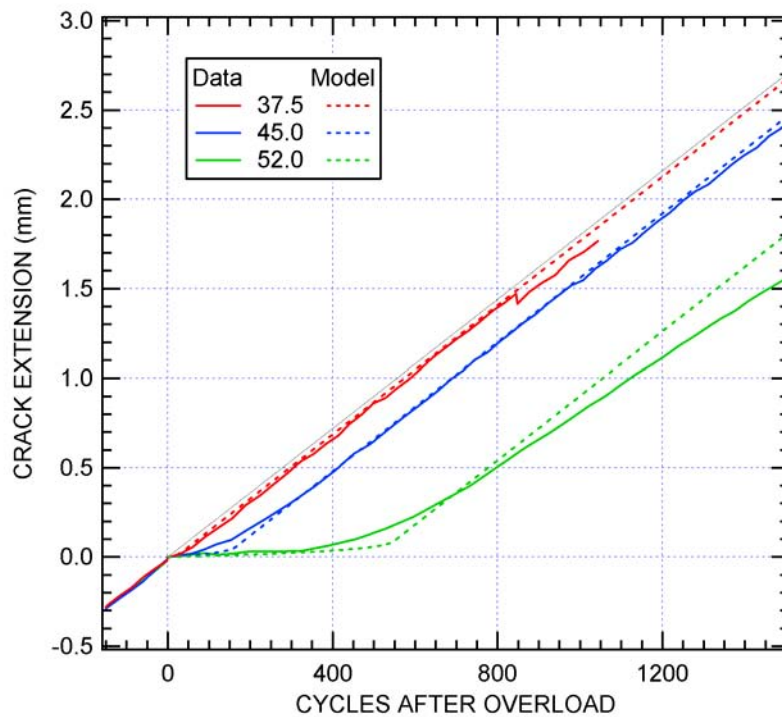


Figure 22. Crack extension as a function of cycles for Specimen 213@0.167 Hz.

Discussion

The Wheeler crack retardation model results in a factor that directly reduces the fatigue crack growth rate and requires an empirical exponent. Widely different exponents are needed to fit the test data, suggesting that the exponent is sensitive to factors other than material variations, for example, the frequency of the loading.

Willenborg [29] proposed an alternative model in which crack retardation results from a reduction in the crack growth driving function, ΔK . He computed a lower “effective” ΔK by considering the residual compressive stress that exists in the crack tip region when the overload is released.

Conclusions

- The crack tip blunting produced by an overload results in a topographic feature on the fracture surfaces.
- The size and shape of the ridge can be measured by confocal laser microscopy or electron stereoscopy.
- The incremental increase of plastic displacement of the overloaded crack front can be obtained by juxtaposing the conjugate topograph surfaces in the configuration of the crack faces during fracture.
- The peak deviation correlates with overload magnitude and crack retardation.
- The overload history of a failed component can be quantitatively deduced from the failure surface.

V. APPLICATION OF DISCRETE COSINE TRANSFORM TO FRACTURE SURFACE ANALYSIS

Fracture surfaces hold information important for prognosis and diagnosis tool development. Remnants of the deformation and microfailure that occurred in the microstructure in the vicinity of a crack front as the crack propagated through a material are exposed on the surface after the crack front has passed. These deformation and microfailure features constitute the end point of the microstructural failure process, and their characteristics can help quantify and verify microstructural failure prognosis models. The feature characteristics are also useful for developing failure diagnosis tools, providing a link to the load history and crack history of the failed component.

However, to be useful in developing prognosis and diagnosis tools, the fracture surface features must be quantified. Various mathematical methods have been applied in attempting to quantify fracture surface features. Unfortunately, the methods usually yield average characteristics of the features, whereas development of physics-based prognosis and diagnosis tools requires numbers and sizes and locations of fracture surface features.

Thus, present methods for extracting quantitative descriptions of failure surface features are inadequate. In seeking a remedy for the situation, we explored the applicability of the discrete cosine transformation (DCT), a technique for decomposing a signal into coefficients of cosine polynomials. The DCT is widely used as a tool in image compression, because of its quick convergence for a very wide range of images, and this property makes it attractive for use as a feature extraction tool in fracture surface analysis. In this section we review the principles of DCT, describe the special methodology we developed for fracture surface analysis, and present the results of DCT application to fracture surfaces.

Background

Researchers interested in building failure prediction tools typically take a continuum approach and have little interest in fracture surface features. Failure analysts, on the other hand, have long appreciated the value of the markings on fracture surfaces, using them to determine the crack initiation site(s), crack growth directions, mode of failure (brittle, ductile, intergranular), and failure mechanism (overload, fatigue, corrosion, etc.) [30]. The results of such feature analyses are usually qualitative, but if quantitative analyses could be performed, additional conclusions on crack growth history and load conditions could be reached.

Methods to quantitatively analyze fracture surfaces have been slow to develop for several reasons [31, 32]. In the first place, a digital representation of a fracture surface image is necessary. SEM photographs were of little use in quantitative analysis until digital video technology was incorporated. Now the contrast image of a fracture surface can be quantified quickly and easily. Furthermore, the topography of a fracture surface can be quickly assessed using stereo SEM or confocal-optics-based scanning laser microscopy, making it possible to characterize digitally the surface roughness—an important but neglected aspect of fracture surfaces.

A second impediment to quantitative fracture surface analysis was the lack of appropriate analysis tools and methodologies. Passoja and Psioda [33], McSwain [34, 35, 36], and Kobayashi and his colleagues [37, 38, 39, 40] applied one- and two-dimensional Fourier transforms to topographic data. Kobayashi also attempted to apply wavelet techniques to fracture surface

topographs. While the resulting elevation power spectrum density vs. wavelength curves discriminated surfaces produced under different load conditions or under different environments, the curves did not provided the location-specific information for features needed for prognosis tool development. In the meantime, a whole new approach to fracture surface analysis was innovated by Kobayashi and his colleagues, who developed a method to reconstruct details of the fracture process and the history of crack growth using digital fracture surface topography. The method, called FRASTA, is described in detail elsewhere [11, 12].

In this work we considered the discrete cosine transform (DCT) and adapted it to characterize fracture surfaces. We applied the methodology to both contrast images and topographic maps of a surface and attempted to both characterize the overall surface and classify specified features as a function of location on the surface. The procedures and results are reported in this section.

The Discrete Fourier and Discrete Cosine Transformations

The discrete cosine transform (DCT) derives from the discrete Fourier transform (DFT) when the signal function to be analyzed is reflected about one of its endpoints.

The discrete Fourier transform (DFT) decomposes a signal, $f(n)$, into coefficients of trigonometric polynomials of the form

$$f(n) = \sum_{n=0}^{N-1} c(n) \cdot e^{2\pi i \cdot n \cdot x(m)} \text{ with } x(m) = m/N \text{ and } m = 0 : N-1 \quad \text{eq. 9}$$

The DFT can be used to characterize a fracture surface by providing information on the frequency content of the surface. For example, a rough surface will have larger components of high frequency content than will a smooth surface.

Although the DFT has been used to characterize fracture surfaces [33-40], it has several significant problems. Foremost is a boundary effect of the signal window. The DFT assumes that the signal being processed is periodic, and repeats the signal consistent with this assumption. Unless the first and last points of the series are equal, there will be a step in the function at the point of repetition. The resulting DFT will contain many high-frequency components needed to characterize the step, which is an artifact of the boundary values, not a true characteristic of the surface.

To improve the DFT characterization it is possible to modify the signal to make the first and last points equal. One common method is to multiply the signal by Hann's window function (a smooth function with end points equal to zero) to make the signal zero at the window boundaries. However, this method can change the function significantly near the boundaries, and may affect the DFT. A second method is to reflect the signal about one of the end points and use the original signal plus the reflection as the new signal, $g(n)$. In this case the first and last points are equal, and the entire content of the original signal is represented. Furthermore, because the new signal is symmetric, the DFT simplifies to a DCT, as described by K.R. Rao and P. Yip [41], and given by

$$G(m) = \frac{1}{\sqrt{N}} w(m) \sum_{n=0}^{N-1} g(n) \cdot \cos(\pi m(2n+1)/2N) \quad \text{eq. 10}$$

with the reconstruction formula given by

$$g(n) = \frac{1}{\sqrt{N}} w(n) \sum_{m=0}^{N-1} G(m) \cdot \cos(\pi m(2m+1)/2N) \quad \text{eq. 11}$$

where $w(n)=1$ if $n=0$ and $\sqrt{2}$ otherwise

The DCT can also be used in the two-dimensional case with all the above properties being preserved. The formula for the two-dimensional DCT is,

$$B(p, q) = \frac{1}{\sqrt{MN}} a(p) a(q) \sum_{m=0}^{M-1} \sum_{n=0}^{N-1} A(m, n) \cos\left(\frac{\pi(2m+1)p}{2M}\right) \cos\left(\frac{\pi(2n+1)q}{2N}\right) \quad \text{eq. 12}$$

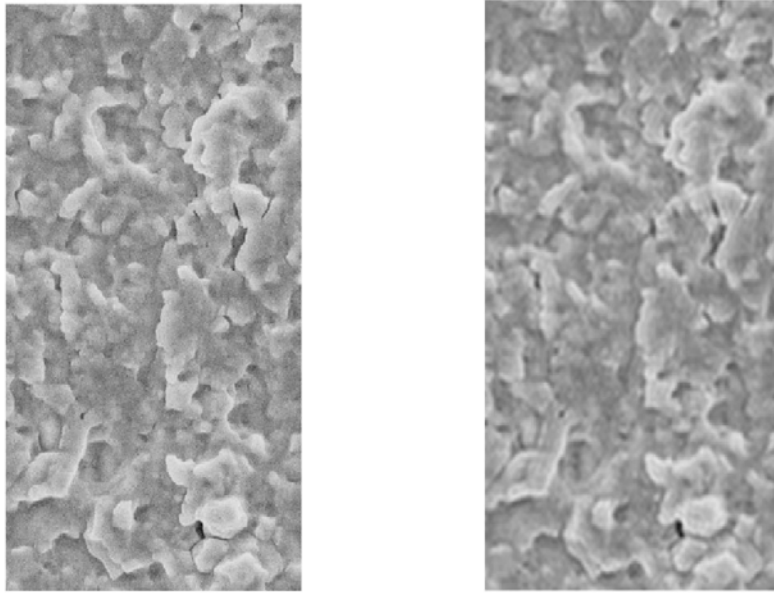
and the reconstruction formula is given by

$$A(m, n) = \frac{1}{\sqrt{MN}} \sum_{q=0}^{M-1} \sum_{p=0}^{N-1} a(p) \cdot a(q) B(p, q) \cos\left(\frac{\pi(2m+1)p}{2M}\right) \cos\left(\frac{\pi(2n+1)q}{2N}\right) \quad \text{eq. 13}$$

with $a(p)$ and $a(q)=1$ if $n=0$ and $\sqrt{2}$ otherwise.

DCT Analysis of an SEM image

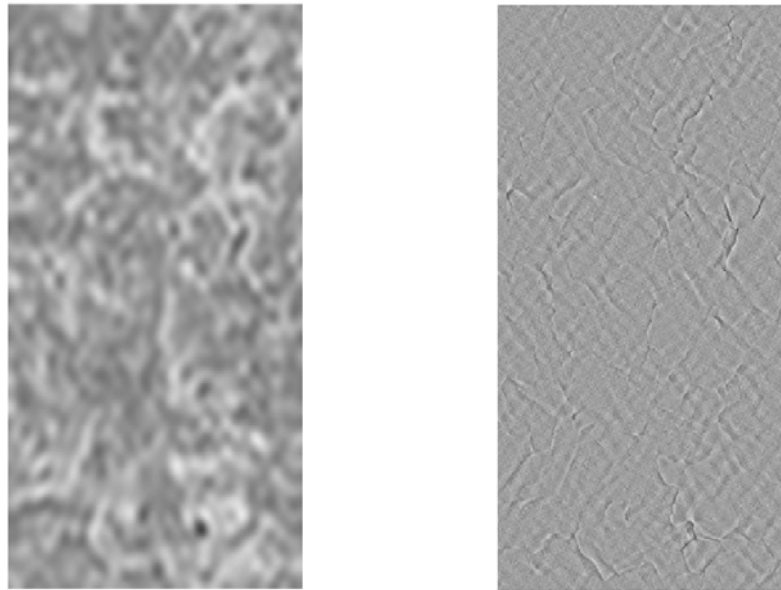
To demonstrate the use of a two-dimensional DCT to characterize a fracture surface, we applied the DCT to an SEM image of a fatigue fracture surface of IN100, a nickel-based superalloy fatigue tested at 650°C. The image, shown in Figure 23a, consists of 512 by 256 pixels, and thus requires 512 by 256 coefficients for the complete DCT. However, to show that the highest frequency components do not add much information, the fracture surface image was reconstructed using only the first 130 by 80 cosine coefficients (a compression factor of approximately 12.6) and, as shown in Figure 23b, the reconstructed image does not look much different than the original.



a) original image of fracture surface b) reconstructed image using 130x80 coefficients

Figure 23. SEM image of fatigue fracture surface of nickel-based superalloy tested at 650 °C.

We can examine the physical significance of specific frequency content of the DCT spectrum on the image. Figure 24a shows the fracture surface image keeping the low-frequency components and filtering out the high frequencies, and Figure 24b shows an image keeping the high-frequency components and filtering out the low frequencies. The image with low-frequency components captures coarse ridges on the fracture surface, whereas the image with high-frequency components shows small steps in the surface and secondary cracks.



a) low frequency components

b) high frequency components

Figure 24. Reconstructed image using different frequency components.

DCT-Analysis of Fracture Surface Topography

The previous demonstration illustrates how efficiently the DCT works to characterize a gray-scale image. The SEM image shows failure features such as voids, ligaments between voids, and cleavage facets. Additional information about the influence of microstructure on failure can be obtained from the topography of the surface. Therefore, we analyze the gray-scale topographic image of a fracture surface, such as the one shown in Figure 25 for a titanium alloy. Here the gray-scale level corresponds directly to the surface elevation as measured by a confocal optics scanning-laser microscope.

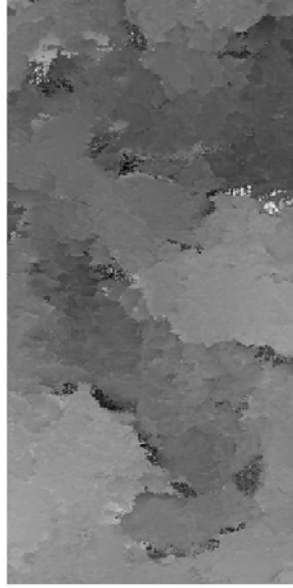


Figure 25. Gray-scale topography image of fatigue fracture surface of titanium alloy.

Performing a DCT analysis of a topographic image can, for example, give a quantitative characterization of the surface roughness. Here we describe a procedure developed to use the DCT to detect and characterize local features on a fracture surface and to identify the specific location of the features.

First we demonstrate the method we use to characterize roughness using a one-dimensional example for clarity. Figure 26 shows three surface profiles with increasing roughness. These profiles were generated using a function of the form,

$$g(n) = 0.2 \left(\sin^2 \left(\frac{2\pi n}{aN} \right) - 0.5 \right) \quad \text{eq. 14}$$

where N , the number of points, is 8 and α is 10, 2, and 0.4, respectively, for the nearly smooth, medium rough, and rough surfaces. These profiles contain just eight data points, and each could be considered as characterizing a short segment of a much longer surface profile.

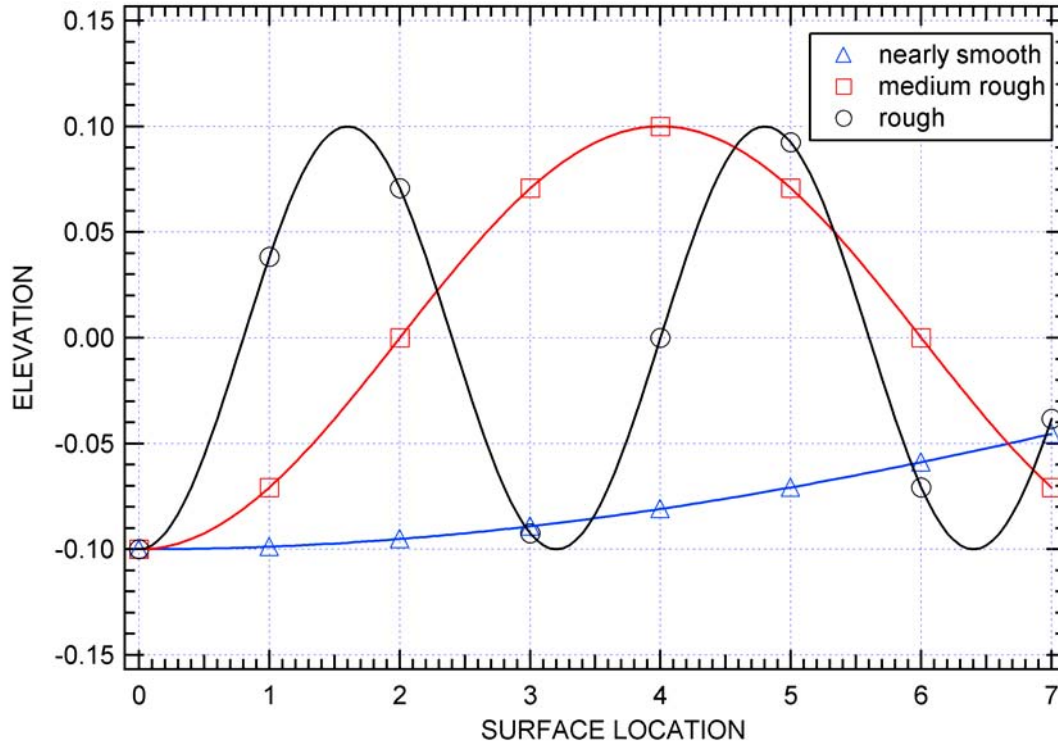


Figure 26. One-dimensional surface topographs.

The DCT coefficients of the surface profiles according to equation 10 above are shown in Figure 27. The amplitudes of the DCT coefficients are shown as functions of the DCT terms, given by the mode number m in equation 10 above (larger m is higher frequency). Note that the DCT terms can be positive or negative, but the rougher the surface, the greater the contribution (in absolute value) of the higher frequencies.

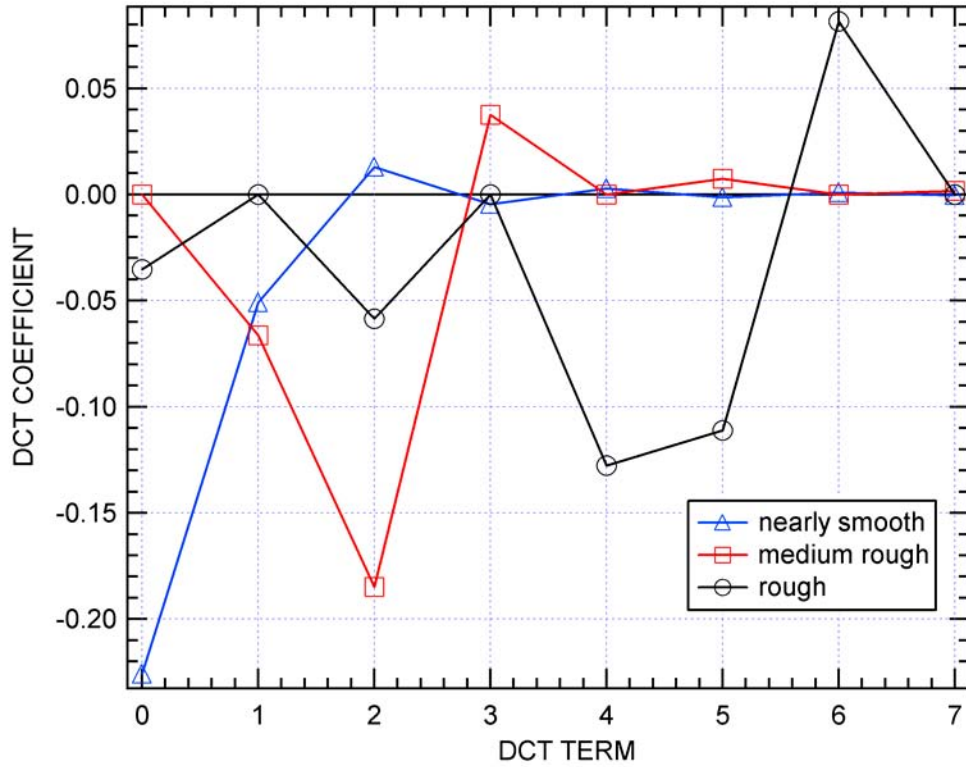


Figure 27. DCT transform of surface profiles.

To get a single quantitative measure of roughness for each surface, we weight the amplitudes of DCT terms by multiplying each term by the corresponding mode number, m , and square that quantity. The resulting weighted terms are shown in Figure 28. The local surface roughness parameter is then taken as the square root of the sum of the squared terms. For the example shown, the local surface roughness values are given in Table 3. The local surface roughness is 0.061 for the nearly smooth profile, 0.39 for the medium rough profile and 0.91 for the rough profile. This procedure clearly distinguishes surface roughness for the example given.

Table 3. Local Surface Roughness Values

Surface	Local surface roughness
Nearly smooth	0.061
Medium rough	0.39
Rough	0.91

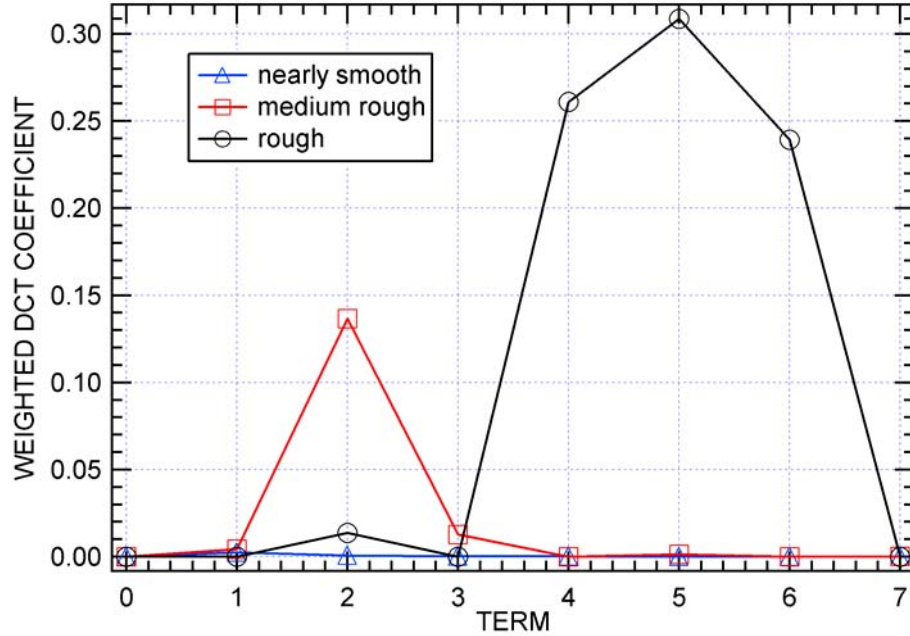


Figure 28. Weighted DCT Amplitude

To enable us to locate a feature such as local roughness on the fracture surface, we divide the fracture surface image into equal-sized subimages and then apply the DCT procedure to each subimage. What results is a scalar roughness measure for each of the subimages. Of course, there is a tradeoff between the number of subimages and the resolution for each subimage. Small subimages give very good resolution for locating the position of a feature on the fracture surface, but limit the amount of resolution for characterizing the feature (in the example above we used eight points for our surface profile). Larger subimages allow us to better distinguish features, but limit the accuracy to locate the feature on the surface. (To allow efficient use of DCT algorithms, the number of pixels in the subimage needs to be a power of 2). After generating a surface roughness value for the subimages, we can identify and classify locations on the fracture surface based on the roughness values. We have found that subimage sizes of 8x8 pixels work well for our application.

For a two-dimensional image of a fracture surface, the procedure is as follows:

1. **Divide the image into equal subimages.** Choose the size of the subimage according to the size of the features of interest. We use a general rule of thumb that the subimage should be large enough to contain about 10 features. Also, for efficiency in the DCT algorithm, the number of pixels should be of size 2^n by 2^n .
2. **Apply the DCT.** Apply the DCT to each of the subimages to get a matrix of DCT coefficients.
3. **Weight the DCT coefficients.** Multiply the matrices containing DCT coefficients by a matrix containing a weighting function, W , that brings out the desired feature. For example, to identify roughness we weight the coefficients by the square root of the sum of the mode numbers, i.e., $W(n, m) = \sqrt{n + m}$. This function emphasizes the

higher frequencies in either direction, such that rougher surfaces will have a greater local surface roughness parameter.

4. **Quantify the feature characteristic.** For example, for local surface roughness, we take the Frobenious norm of each of the matrices of the weighted DCT coefficients. The Frobenious norm is defined as the l^2 norm of a square of l^2 norms of each column of a matrix. (Note: Although other norms also work well, the Frobenious norm seems to be the most logical because it involves both columns and rows and considers all the frequencies in the same manner.) The Frobenious norm gives for each subimage a single scalar value we call the local surface roughness. The value of local surface roughness characterizes the surface roughness at the location of the sub-image.
5. **Locate the features of interest.** Rank and characterize the feature values of the subimages. For example, for local surface roughness, we identified all the subimages with roughness values less than the average value minus one half of a standard deviation, and those subimages with a roughness value greater than the average value plus one half of a standard deviation. These correspond to smooth areas and rough areas. The remaining subimages are areas of average roughness.

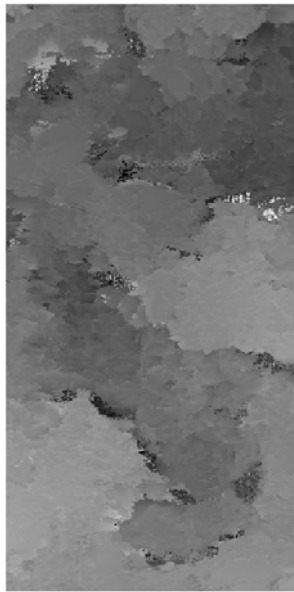
Figure 29 shows a gray-scale topographic image of a fracture surface of a titanium alloy (Figure 29a) along with identified areas of low (Figure 29a), intermediate (Figure 29b) and high (Figure 29c) local surface roughness. A visual comparison of the identified regions with the gray-scale levels of the topographic image of the fracture surface shows that the smooth and rough areas are well identified and their locations on the fracture surface are clearly established.

Discussion

The discrete cosine transform appears to be an efficient algorithm for analyzing fracture surfaces. Convergence is quick, and only a few coefficients are needed to capture image characteristics.

The procedure we developed not only identifies selected fracture surface features, but also identifies their location on the surfaces. Fractographic features of any specified shape can be selected for analysis by taking appropriate weighted norms of the DCT spectrum. The feature size of interest can be selected by choosing the size of the subimages.

We expect to use the DCT analysis method to generate data for developing physics-based prognosis and diagnosis tools. Information on microfailure modes can be obtained concurrently with microstructure influences by combining DCT results from SEM images with those from fracture surface topographs. A next step is to apply statistical analyses to the DCT spectrum data.



a) original topograph



b) areas of low roughness



c) areas of intermediate roughness



d) areas of high roughness

Figure 29. Original topograph image and areas of low, intermediate, and high local surface roughness.

Conclusions

1. The DCT analysis shows promise for extracting and quantifying surface features on fracture surface images.
2. By dividing the image into subimages and analyzing each subimage separately, the DCT analysis can relate feature characteristics to specific locations on the fracture surface.
3. By choosing appropriate selection criteria on the DCT spectrum, fracture surface features such as cleavage facets, ductile dimples, and exposed grain surfaces can be identified and located.
4. The DCT analysis procedure is efficient and can be automated.
5. The DCT analysis appears to be an enabling procedure for developing physics-based prognosis and diagnosis tools.

VI. REFERENCES

- 1 May, R., Keynote address at the 5th National Turbine Engine High Cycle Fatigue Conference, Sheraton San Marcos Hotel, Chandler, AZ, March 7-9, 2000.
- 2 <http://www.lstc.com>.
- 3 L. Seaman, J.W. Simons, and D.A. Shockey, "A Microcracking Fatigue Model for Finite Element Analysis," *Advances of Local Fracture/Damage Models for the Analysis of Engineering Problems*, J. H. Giovanola and A. J. Rosakis, Eds., Book No. H00741, pp.243-255, 1992.
- 4 Miner, R.V., J. Gayda, and R.D. Maier, "Fatigue and Creep-Fatigue Deformation of Several Nickel-Base Superalloys at 650C," *Met. Trans. A*, vol. 13A, 1755-1765, Oct 1982.
- 5 Cowles, B.A., D.L. Sims, J.R. Warren, and R.V. Miner, *Trans ASME*, vol. 102, pp. 356-63, 1980.
- 6 C. Mercer, A.B.O. Soboyejo, and W.O. Soboyejo, "Micromechanisms of fatigue crack growth in a single crystal inconel 718 nickel-based superalloy," *Acta Mater.*, Vol 47, No. 9, 1999, p. 2727-2740.
- 7 C. Mercer, A.B.O. Soboyejo, and W.O. Soboyejo, "Micromechanisms of fatigue crack growth in a forged Inconel 718 nickel-based superalloy," *Mater. Sci. Eng. A270*, 1999, p. 308-322.
- 8 Repetto, E.A. and M. Ortiz, "Micromechanical model of cyclic deformation and fatigue-crack nucleation in f.c.c. single crystals," *Acta Materialia* 45(6): 2577-2595, 1997.
- 9 Harren, S.V., H.E. Deve, R.J. Asaro, "Shear band formation in plane strain compression," *Acta Metallurgica* 36(9): 2435-2480, 1988.
- 10 Morrison, D.J. and V. Chopra, "Cyclic Stress-Strain Response of Polycrystalline Nickel," *Materials Science and Engineering A177*: 29-42, 1994; (b) Morrison, D.J. and J.C. Moosbrugger, "Effects of Grain Size on Cyclic Plasticity and Fatigue Crack Initiation in Nickel," *International Journal of Fatigue* 19(1): S51-S59, 1997.

- 11 Kobayashi, T., and D.A. Shockey, "FRASTA—A New Way to Analyze Fracture Surfaces, Part I: Reconstructing Crack Histories," *Advanced Materials and Processes*, vol 140 (5), 28-34, 1991.
- 12 Kobayashi, T., and D.A. Shockey, "Fracture Analysis Via FRASTA, Part 2: Determining Fracture Mechanisms and Parameters," *Advanced Materials and Processes*, vol 140 (6), 24-32, 1991.
- 13 K. Sadananda, A.K. Vasudevan, R.L. Holtz, and E.U. Lee; "Analysis of Overload Effects and Related Phenomena," *International Journal of Fatigue* Vol. 21 pp S233-S246 (1999).
- 14 R.H. VanStone and D.C. Slavik, "Prediction of Time-Dependent Crack Growth with Retardation Effects in Nickel Based Alloys, Fatigue and Fracture Mechanics," 31, ASTM STP 1289, ASTM, pp. 405-426 (2000).
- 15 Y. Murakami, N. Shiraishi, and K. Furukawa, "Estimation of service loading from the width and height of fatigue striations of 2017-T4 Al alloy," *Fatigue Fract. Engng. Mater. Struct.* Vol. 14, No. 9, 1991, p. 897-906.
- 16 K. Furukawa, Y. Murakami, and S. Nishida, "A method of predicting service load from the width and height of striation," *J. of the Soc. Of Materials Science Japan*, Vol. 45, No. 3, 1996, p. 340-345.
- 17 H. Kaneko, H. Ishikawa, T. Konishi, M. Yamada, "Study on estimation methods of applied stress using fractography analysis," *Mitsubishi Heavy Industries, Ltd. Technical Review*, Vol. 38, No. 3, 2001 p. 156-160.
- 18 N. Ranganathan, M. Benguediab, G. Henaff, and F. Adiwijayanto, "Quantitative Fracture Surface Analysis of Fatigue Crack Propagation Under Variable Amplitude Loading," *American Society for Testing and Materials*, Philadelphia, 1994, p. 71.
- 19 A. Varvani-Farabani and T.H. Topper, "The effect of periodic compressive overloads on the crack surface roughness and crack growth rate of short fatigue cracks in 1045 steel," *Proceedings Int. Conf. on Fracture and Fatigue Threshold*, Pennsylvania, 1996.
- 20 G.A. Kardomateas and R.L. Carlson, "Predicting the effects of load ratio on the fatigue crack growth rate and fatigue threshold," *Fatigue & Fracture Materials & Structures*, 21, 1998, p. 411-423.
- 21 G.S. Pisarenko, A.Y. Krasowsky, V.A. Vainshtock, I.V. Kramarenko and V.N. Krasiko, "The combined micro- and macro-fracture mechanics approach to engineering problems of strength," *Engineering Fracture Mechanics*, Vol. 28, No. 5/6, 1987 p. 539-554.
- 22 M. Srinivas, S.V. Kamat, and P. Rama Rao, "A fractographic technique for the estimation of initiation fracture toughness J_{Ic} for ductile Materials," *Journal of Testing and Evaluation*, JTEVA, Vol. 22, No. 4, 1994, p. 302-308.
- 23 P.R. Sreenivasan, S.K. Ray, S. Vaidyanathan, and P. Rodriguez, "Measurement of stretch zone height and its relationship to crack tip opening displacement and initiation J-value in an AISI 316 stainless steel," *Fatigue Fract. Engng Mater. Struct.* Vol. 19, No. 7, 1996 p. 855-868.

- 24 J. Stampel, S. Scherer, M. Berchthaler, M. Gruber, and O. Kolednik, "Determination of the fracture toughness by automatic image processing," *International Journal of Fracture*, 78, 1996, p. 35-44.
- 25 A.J. Krasowsky and V.A. Stepanenko, "A quantitative stereoscopic fractographic study of the mechanism of fatigue crack propagation in nickel," *International Journal of Fracture*, Vol, 15, No. 3, 1979 p. 203-215.
- 26 A.J. Krasowsky and V.A. Vainshtok, "On a relationship between stretched zone parameters and fracture toughness of ductile structural steels," *International Journal of Fracture*, Vol. 17, No. 6, 1981 p. 579-592.
- 27 A. A.Wells, "Unstable Crack Propagation in Metals: Cleavage and Fast Fracture," *Proceedings of the Cranfield Crack Propagation Symposium*, England, Cranfield, U.K., Vol. 1, 1961, pp. 210-230.
- 28 O.E. Wheeler, "Spectrum Loading and Crack Growth," *Transactions of the ASME* (March 1972).
- 29 J. Willenborg, R.M. Engle, and H.A. Wood, "A Crack Growth Retardation Model Using an Effective Stress Concept," *Technical Memorandum 71-1-FBR 7784 to the Air Force Flight Dynamics Laboratory* (January 1971).
- 30 ASM Handbook, Volume 12, *Fractography*, 1987, American Society of Materials International (1987).
- 31 C. Brooks and B.L. McGill, "The application of scanning electron microscopy to fractography," *Materials Characterization*, Vol. 33, 1994, p. 195-243.
- 32 J. Russ, "Computer-assisted image analysis in quantitative fractography," *JOM*, 1990, p. 16-19.
- 33 D. E. Passoja and J. A. Psioda, "Fourier Transform Techniques—Fracture and Fatigue," in *Fractography and Materials Science*, ASTM STP 733, L. N. Gilbertson and R. D. Zipp, Eds., ASTM 355 (1981).
- 34 R. H. McSwain, "Digitized Fractographic Image Analysis," Ph.D. thesis, University of Florida, Gainesville, FL (1985)
- 35 R.H. McSwain, and Gould, R.W., "Analysis of a Helicopter Blade Fatigue Fracture by Digital Fractographic Imaging Analysis," *Proceedings of the International Conference and Exposition on Fatigue, Corrosion Cracking, Fracture Mechanics and Failure Analysis*, Edited by V. S. Goel, American Society for Metals, Salt Lake City, UT, December 1985, pp. 87-91.
- 36 R. W. Gould and R. H. McSwain, "Fractographic Feature Identification and Characterization by Digital Image Analysis," in *Fractography of Modern Engineering Materials: Composites and Metals*, ASTM STP 948, 263-292 (1987).

- 37 T. Kobayashi, D. A. Shockey, C. G. Schmidt, R. W. Klopp, "Assessment of Fatigue Load Spectrum from Fracture Surface Topography," *Int. J. Fatigue* 19(1), S237-S244 (1997)
- 38 C. G. Schmidt, T. Kobayashi, D. A. Shockey, and T. H. Flournoy, "Correlation of Fracture Surface Topography with Fatigue Load History," *Proceedings of the International Committee on Aeronautical Fatigue 1997*, Edinburgh, Scotland (June 16-20, 1997).
- 39 T. Kobayashi and D. A. Shockey, "On the Relationship between Fracture Surface Roughness and Fatigue Load Parameters," *International Journal of Fatigue*, 23 S135-S142 (2001).
- 40 T. Kobayashi and D. A. Shockey, "Fast Fourier Transform Analysis of Fracture Surface Topography," *FATIGUE 2002*, *Proceedings of the Eighth International Fatigue Congress*, Stockholm Sweden 3069-3076 (June 3-7, 2002).
- 41 K. R. Rao and P. Yip, "Discrete Cosine Transform- Algorithm, Advantages, Application," Academic Press, London, UK, 1990.